Cold dwell fatigue analyses integrating crystal-level strain rate sensitivity and microstructural heterogeneity

Yang Liu*, Suki Adande, Thomas Benjamin Britton and Fionn P.E. Dunne

Department of Materials, Imperial College London, London SW7 2AZ, United Kingdom

Abstract

Cold dwell fatigue remains an important life-limiting factor in aircraft engine titanium alloys. Microstructure-level creep and stress accumulation during each loading cycle are controlled by strain rate sensitivity. Here, an integrated experimental and computational framework is used to link crystal-level slip properties to microstructure-sensitive cold dwell debit of a forged rotor graded Ti-6Al-4V alloy. Slip strengths and anisotropic strain rate sensitivities are extracted from micro-pillar compression tests for different slip systems, incorporated within α+β microstructurally-faithful polycrystal representations. Dwell and non-dwell cyclic loading in alloy Ti-6Al-4V are investigated for two differing microstructures, and the cycles to failure predicted based solely on the crystal c-axis tensile strength, and the dwell debit quantified. The dwell effect is predicted to diminish to zero below a peak applied stress of about 790 MPa in the alloy studied.

1. Introduction

Titanium alloys are widely used for aircraft components for their excellent mechanical properties and corrosion resistance. Cold dwell fatigue in titanium alloys has drawn attention over many years because of reported dwell-related aero-engine failures [1,2]. For titanium-based alloys, dwell fatigue is cyclic loading which includes a stress dwell (a hold at load) within the fatigue cycle, and this has been found to give a substantial lifetime reduction which has been called the dwell debit. A material is considered to be dwell sensitive if when tested in fatigue, there is a substantial reduction in the number of cycles to failure for tests containing a stress dwell. Bache et al. found that the dwell debit is reduced by applying lower peak hold stress [3]. Ozturk et al. [4] using CP modelling also demonstrated that the number of cycles to nucleate facets increases with decreasing dwell stress. Facet crack nucleation in hexagonal closed packed (HCP) titanium crystals is argued to be responsible for the early service failure of near-α titanium alloys [5]. Hasija et al. found that a combination of local crystallographic orientations with respect to the loading direction caused load shedding during the dwell period [6]. Load shedding refers to the redistribution of stress from a soft creeping grain to an adjacent elastic hard grain. During the load hold, this local creep behaviour results in high grain boundary stresses [7] and may induce the subsequent crack nucleation.

Much work has been carried out to understand the mechanistic basis of the load shedding phenomenon. Hasija et al. first reported the stress redistribution from soft to hard-orientated grains in single α phase Ti-6Al using crystal plasticity (CP) modelling [6]. High energy X-ray diffraction combined with crystal plasticity modelling has been used to capture the rate sensitivity and residual stress within each grain for Ti-7Al [8]. Huang et al. demonstrated the load partitioning between the soft (matrix) and hard (precipitate) grains due to the creep behaviour using in-situ neutron diffraction techniques [9]. Sinha et al. studied near-α Ti-6242 alloy and have shown the prismatic slip accumulated in the soft grain results in dislocation pileups and hence inducing elevated stress fields more likely to initiate cracks on basal planes in the adjacent hard grain [5,10]. Modelling work [11–13] has shown progressive local stress

development under dwell fatigue loading at room temperature using homogenised α phase CP models incorporating hard-soft grain orientation combinations.

Slip transfer analysis at α/α grain boundaries has been carried out by Joseph et al. [14] who observed direct dislocation transfer in adjacent similarly oriented grains but dislocation pileups at soft-hard grain boundaries. In modelling studies, Zheng et al. concluded that pile-up stress is the key driver of direct slip transfer and dislocation transmission, whereas, for lower pile-up stress, dislocation pile-ups occur but without slip transfer. This conclusion was found to remain the case for both α/α grain boundaries and α/β phase boundaries [15].

Strain rate sensitivity has been argued as a key factor in dwell fatigue and the resulting facet nucleation [7,16]. Both experimental and modelling studies in alloys Ti-6242 and Ti-6246 show that the former gives rise to much higher cold creep than that of Ti-6246, and their dwell temperature sensitivities have been investigated based on the thermally activated slip and reduction of slip strength anisotropy with increasing temperature [7]. Experimental micro-pillar methodologies integrated with crystal plasticity modelling have been developed in order to extract α and β phase properties including the slip system strengths and strain rate sensitivities. These approaches have been used to measure the anisotropic basal and prism slip strengths and strain rate sensitivities of single crystal α for alloy Ti-6242 at 20 °C together with those of the beta phase [16]. The origin of the differing creep responses arising in the Ti-624x alloys has been argued to be related to α-β microstructures [16] which are developed as a result of processing route. With different cooling rate, dual phase titanium alloys develop distinct microstructures which can include equiaxed α grains with dispersed or grain boundary β, duplex primary α and α-β colony structures, Widmanstätten and basketweave structures (containing multiple α variants). Basketweave structures are found in experimental studies to be dwell insensitive [17–19], and have greater creep resistance than bimodal microstructures. Modelling studies based on the α and β phase properties extracted from micro-pillar testing have explained these experimental observations [20] and provided a systematic comparison of the creep and dwell responses anticipated as a function of the important dual phase titanium microstructures which arise from processing.

Macrozones or microtextured regions (MTRs) are widely observed within titanium components, which are thought to be important for strain localization, dwell debit increase and corresponding crack nucleation [21–27]. An agreed definition of these regions of common orientation remains unclear, but they are sometimes considered to be an 'effective structural unit' [28] with given dominant crystallographic orientation with common basal plane or Burgers vector, often with a morphology of high aspect ratio, and with highest dimension of order mm in length. Our former study [27] shows that macrozones of Ti-6Al-4V, which have aspect ratio larger than four and basal poles within 15° of remote loading direction, lead to much higher stress redistribution (load shedding). In this paper, it is argued that the single-crystal slip rate sensitivities are needed to better describe local slip localisation, creep accumulation and stress redistribution in polycrystal behaviour. The Burger Orientation Relationship (BOR) between neighbouring α/β phases developed during processing is also important and crystal plasticity simulations have shown that phase boundaries (give the BOR) play a very significant role in local creep, which results in higher creep resistance within basketweave structures (containing multiple α variants) compared to globular, colony, or Widmanstätten structure [20,29].

Together these observations lead us to the hypothesis that dwell debit in titanium alloys depends on the intrinsic strengths and strain rate sensitivities of the constituents within the α and β phases, as well as their relative shapes, sizes and BOR within the dual phase microstructure [29]. In turn, this suggests that the results of [30], which show dwell sensitivity

differences between Ti-6246 and Ti-6262 (where the molybdenum content is different), is controlled by the structural unit sizes, i.e. the microstructure, and not the intrinsic chemistry effects within each phase.
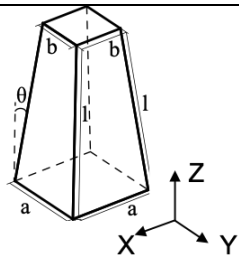
The purpose of this study is to establish microstructurally faithful models, with explicit representation of both α and β phases, to provide mechanistic insight into dwell sensitivity of a representative forged rotor grade alloy, Ti-6Al-4V. To calibrate these models, we use direct extraction of single-crystal α and β slip properties from micro-pillar testing to facilitate determination of anisotropic slip-system rate sensitivities. These models are used to quantify micro-texture cyclic creep and load shedding and to predict both dwell fatigue life based on single crystal c-axis tensile strength and dwell debit corresponding to given microstructures. In addition, the stress threshold below which dwell fatigue does not occur can be predicted in principle using these models. This methodology provides a route to establish the dwell fatigue sensitivity of any arbitrary titanium alloy with knowledge of its microstructure and direct extraction of the intrinsic α and β phase rate sensitive mechanical properties.

In the following sections, first we present measurement of properties from the micro-pillar tests. Next, we develop two key morphology- and texture-representative α+β microstructure models. We draw this together with microstructurally faithful dwell and non-dwell fatigue analyses, including quantification of cyclic creep and load shedding. This enables us to generate S-N life curves and predict dwell debits for the two microstructures.

2. Methods: pillar compression and crystal plasticity modelling

We follow the approach of [31] to cut and test micro-pillars. As received Ti-6Al-4V was heat treated 1040°C above the α→β transus temperature and held for 8 hours and then slow cooled at 1 °C/min to room temperature. The sample was metallographically polished finishing with a pH balanced 0.05 μm colloidal silica. This was suitable for electron backscatter diffraction (EBSD) analysis, and Figure 1 presents the orientation map with respect to the sample known from prior EBSD calibration using the procedure in [32]. This EBSD map was used to select two grains for micro-pillar fabrication. The grains were selected such that single slip of the <a> basal and <a> prismatic slip systems were activated. Micro-pillars were fabricated using focused ion beam (FIB) machining, with a target square top cross section of 2×2 μm^2, and a height of ~ 5 μm. FIB trenching was used to ensure that a sufficient volume subsurface was of the same crystal structure. Three pillars were machined in grain with specific orientation to give prismatic slip, and two pillars to give basal slip, which were subsequently measured in the SEM to provide geometries and dimensions (including taper angles) which are presented in Table 1. The magnification of the microscope was verified by a standard sample and the uncertainty exists in the measurement of the cross-section area and the height containing ~2% and ~1% variations. The contact misalignment between the top surface of the pillar and the flat punch would affect the load response and change stress state within the pillar. Here, the indenter system and FIB milling were optimised to reduce alignment error, such that pillars were loaded uniaxially with their primary axes parallel to the loading and normal to the sample surface under displacement control. The top punch with tip diameter of 20 μm is much greater than the pillar top width and the uncertainty within displacement/force measurement would be less than 1%. The FIB sputtering process during milling may lead to slightly pillar taper angle of ~2º [33,34]. Under loading, the slip was confined to occur in the top region of the pillars under these geometries, with smaller cross-sectional area leading to higher stress. The pillar geometries were fully captured in the associated crystal plasticity modelling such that accurate calculation of pillar stresses could be obtained, from which the slip system resolved shear stresses to activate slip could be extracted.

Table 1 Micro-pillar dimensions and crystallographic orientations

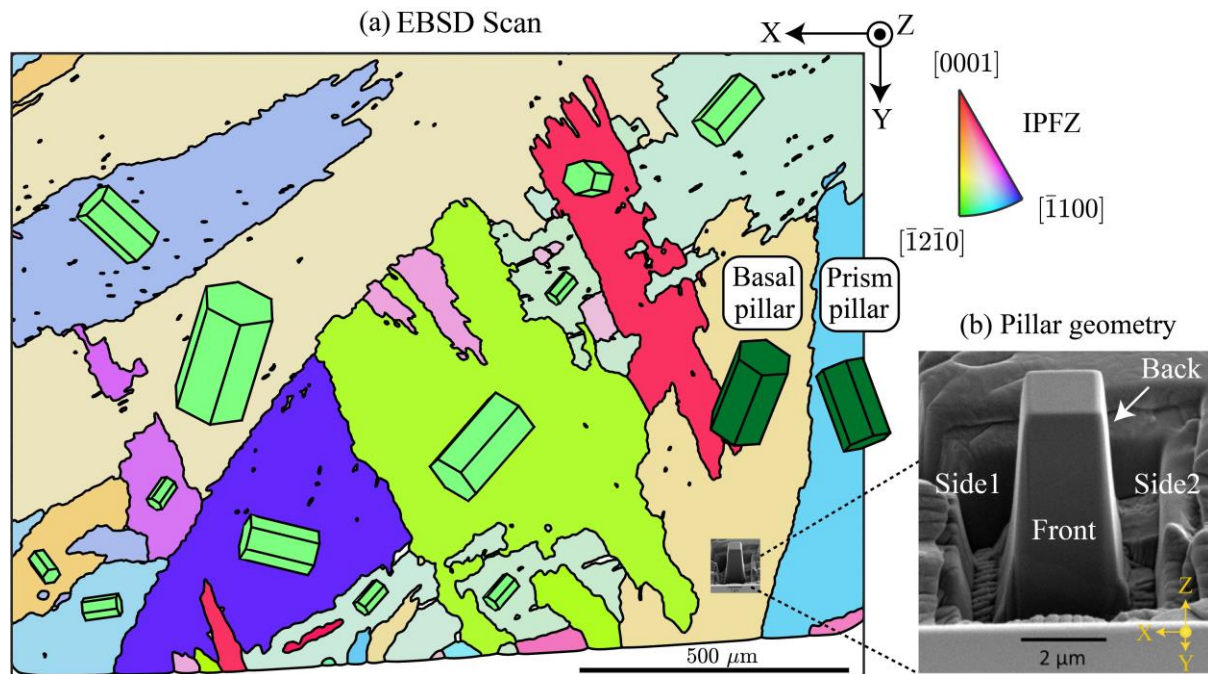| Pillar geometry		Prismatic pillar			Basal pillar	
		P1	P2	P3	B1	B2
	Displacement rate (μm/s)	0.054	0.012	0.0008	0.058	0.0008
	a (μm)	3.08	2.70	3.06	2.80	2.50
	b (μm)	1.85	1.60	1.69	1.75	1.77
	l (μm)	5.22	5.27	5.30	5.88	5.36
	θ (°)	5.67	5.99	7.43	5.12	3.90
	Bunge's Euler angle (°)		[20,99,19]			[158,126,171]

Figure 1. The heat treated Ti-6Al-4V microstructure showing (a) grain morphology and crystallography from EBSD with chosen locations for machining pillars with high basal and prismatic Schmid factor. (b) A typical pillar with sides labelled is shown in EBSD scan [35]. Z points out of the page of the EBSD scan.

Mechanical testing was performed inside a SEM using an Alemnis nanoindenter. This is a displacement-controlled system, actuated with a piezoelectric stack and the force is measured using a load cell. A 10 μm diameter diamond flat punch was used to compress the pillars. The pillars were deformed with three different displacement rates to a maximum of ~5% engineering strain ($\varepsilon_{eng}=\Delta d/d_0$, $d_0=l\cos\theta$ the initial height; Δd the applied displacement). The displacement control is applied at the top centre of the pillars at a constant displacement rate until a peak 5% engineering strain is achieved. Then the displacement is held constant for 120s during which force relaxation is expected to occur. Different displacement rates are applied on both basal and prismatic pillars, and detailed in Table 1.

The experimental load-displacement data is modelled using a geometrically faithful crystal plasticity model, including the fixed base, sample taper and boundary conditions from the flat punch. Plasticity is modelled using a strain rate sensitive dislocation-based crystal plasticity model, introduced originally in [36]. To recap, in the model, finite strain theory is used and multiplicative decomposition of total deformation gradient $\mathbf{F}$ is

$$\mathbf{F} = \mathbf{F}^e \mathbf{F}^p \tag{1}$$

where $\mathbf{F}^e$ and $\mathbf{F}^p$ are the elastic and plastic deformation gradients, respectively. This is incorporated within a rate-based formulation with a plastic velocity gradient, $\mathbf{L}^p$ given by

$$\mathbf{L}^p = \dot{\mathbf{F}}^p (\mathbf{F}^p)^{-1} \tag{2}$$

and may be written in terms of slip system shear rates as

$$\mathbf{L}^p = \sum_\alpha \dot{\gamma}^\alpha \, \mathbf{m}^\alpha \otimes \mathbf{n}^\alpha \tag{3}$$

where $\mathbf{m}^\alpha$ and $\mathbf{n}^\alpha$ are slip direction and normal of the αth slip system. $\dot{\gamma}^\alpha$ is the slip (shear) rate which is obtained from the Orowan equation

$$\dot{\gamma}^\alpha = \rho_m \nu (b^\alpha)^2 \exp\left(-\frac{\Delta F^\alpha}{kT}\right) \sinh\left(\frac{\Delta V^\alpha}{kT}(\tau^\alpha - \tau_c^\alpha)\right) \tag{4}$$

where ρ_m is the density of mobile dislocations, ν the frequency of dislocation jumps, b^α the magnitude of the Burgers vector, k the Boltzmann constant and T the temperature in Kelvin. Specifically, ΔF^α is the thermal activation energy for pinned dislocation escape from obstacle locations which effectively sets the time constant associated with the strain-rate sensitivity range, and ΔV^α is the activation volume which governs the magnitude of the strain rate sensitivity over the strain rate range considered. Determined by fitting to the experimental data, ΔV^α and ΔF^α control the strain-rate/creep sensitivity are determined independently for basal and prismatic slip. This is used to capture the intrinsic anisotropic strain rate sensitivity in the independent slip systems (as they are likely to be different, as indicated in prior work [37]).

τ^α and τ_c^α are the resolved shear stress and critical resolved shear stress, for the α slip system respectively, such that slip occurs once $\tau^\alpha \geq \tau_c^\alpha$. The magnitude of τ_c^α increases with hardening, here taken to be

$$\tau_c^\alpha = \tau_{c,0}^\alpha + G_{12} b^\alpha \sqrt{\rho_{GND} + \rho_{SSD}} \tag{5}$$

where, $\tau_{c,0}^\alpha$ is the initial critical resolved shear stress, G_{12} the shear modulus component, ρ_{GND} the geometrical necessary dislocation (GND) density, and ρ_{SSD} the statistically stored dislocation (SSD) density. The initial GND density is zero since no lattice curvature exists in the initial single crystal pillars and the initial SSD density is set to be 10^{10} m^{-2}, which is compatible with the initial stored dislocation density range reported before [38–40]. The evolution of ρ_{GND} is computed from the Nye tensor curl($\mathbf{F}^p$) based on L2 least squares minimisation and

$$\sum_\alpha \mathbf{b}^\alpha \otimes \boldsymbol{\rho}^\alpha = \text{curl}(\mathbf{F}^p) \tag{6}$$

where, $\boldsymbol{\rho}^\alpha$ is the dislocation density vector.

The evolution rate of ρ_{SSD} is described phenomenologically as

$$\dot{\rho}_{SSD} = \gamma_s \dot{\bar{\varepsilon}}^{\,p}$$

where $\dot{\bar{\varepsilon}}^{\,p} = \sqrt{2/3(\dot{\varepsilon}_{ij}^p \dot{\varepsilon}_{ij}^p)}$, and γ_s is the hardening coefficient for statistically stored dislocation density, which controls the strength increase during the pillar compression. The calibrated γ_s from the prismatic pillar was checked against that in the basal pillar to verify its consistency and validity in describing corresponding hardening in both crystallographies.

3. Pillar results

The micro-pillar tests have been designed to facilitate property extraction. The methodology utilized has been fully detailed in the literature [41] so a brief outline is presented here. The elastic part of the force-displacement measurements enables calibration of the elastic constants and frame compliance and estimation of the latter is given in Appendix A. Slip after yielding enables determination of the initial CRSS values, which are refined slightly once the strain rate sensitivity is taken into account. The displacement holds and stress relaxation enables calibration of the activation volume and energy. We note that the geometry, crystal orientation and displacement time boundary conditions of the experiment are replicated directly in the model. Multiple pillar compression rates were carried out for both basal and prismatic pillars.

The modelling geometry and mesh is shown in Figure 2 (a), which includes the pillar cut from the single phase α region, the titanium base under the pillar (and with the same crystallographic orientation) and the adhesive used to locate the specimen within the loading frame. The mesh type is C3D20R with 8 integration points and a mesh convergence study is given in Appendix B. Z-direction displacement control is applied on the upper surface of the pillar and the bottom of the glue section is fully constrained in the Z-direction at its base. The glue substrate is fixed at a single central point only at its bottom-centre to locate its position in the XY plane. The mesh element size within the pillar is controlled at 0.35 μm to ensure accurate elasto-plastic response and is about 10 times finer than that of most of the base and glue regions, within which a uniform deformation state exists. The model crystallographic orientations are chosen to replicate the experimental measurements indicated in Figure 2 (b).

The pillar base (along with the pillar itself) must be modelled with anisotropic elasticity, as there is significant compliance difference between the two pillars resulting from their orientations, shown in Figure 2 (c). The isotropic elastic modulus of cyanoacrylate based adhesive glue is found to be 9.1 GPa, within the modulus range 3 - 15 GPa, published by the manufacturer [42] with Poisson ratio of 0.3. The calibrated elastic properties of the pillar and base material are shown in Table 2.
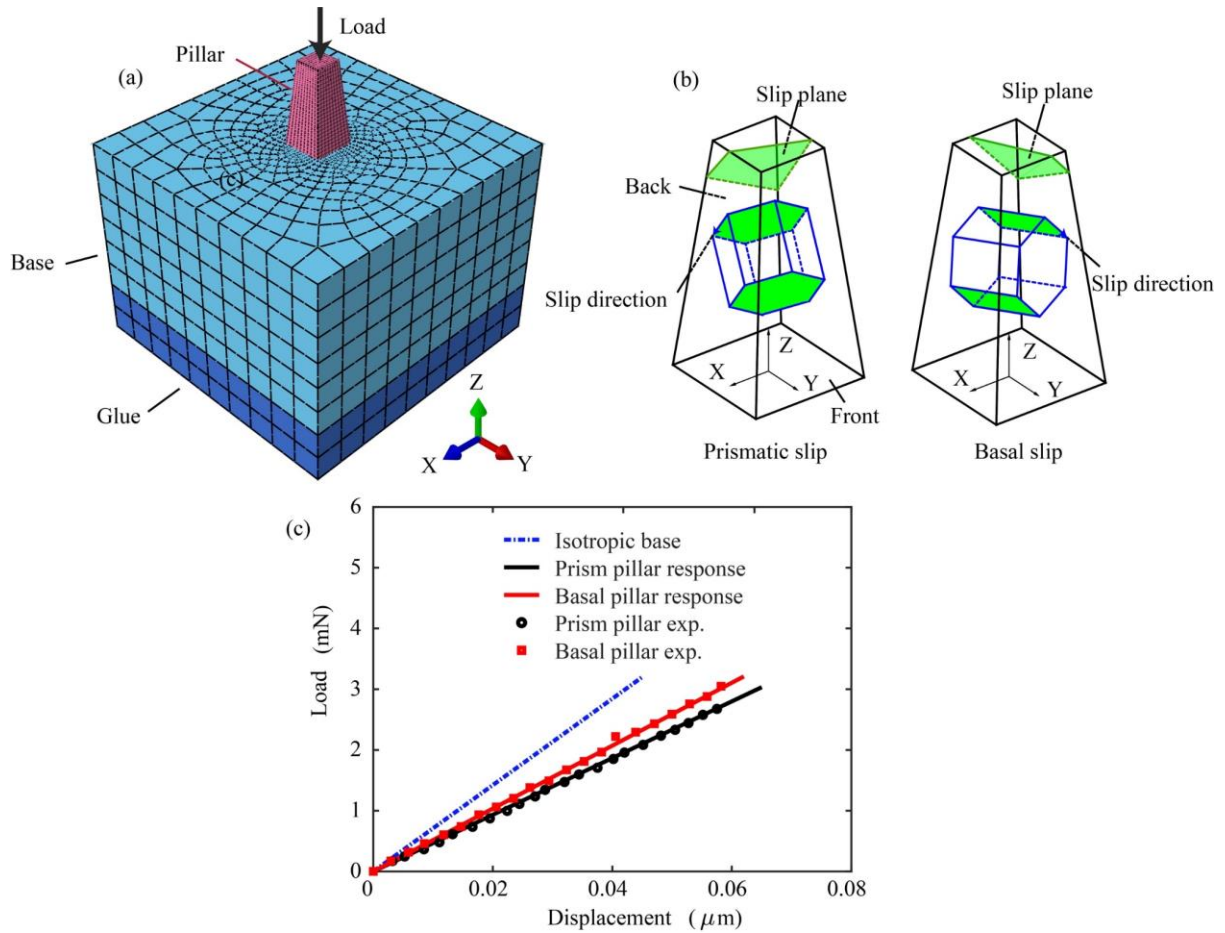
Figure 2 Crystal plasticity model micro-pillar set-up (a) Model mesh and geometry including the pillar, base and cyanoacrylate-based epoxy glue. Displacement is applied on top of the pillar and the base of the glue region is fully constrained in the Z-direction. (b) Pillar crystallographic orientations selected to give prismatic and basal slip. (c) Calibrated elastic pillar force-displacement responses capturing the base anisotropic elasticity. P1 and B1 with vertical engineering strain rate of 0.01/s are the prism and basal pillars shown in (c).

The extraction of slip strengths τ_c^α, hardening coefficient γ_s and strain rate sensitivities (ΔV^α and ΔF^α) for separate prism and basal systems, respectively, involves (i) trial model prediction (based on properties for related alloys), (ii) parameter modification, and (iii) verification. Each pillar subject to differing displacement rates is modelled individually to ensure accurate representation of pillar geometry, with appropriate specification crystal orientation from the EBSD measurement.

The imposed displacement loading histories of prismatic pillars P1-3 subjected to the different displacement rates indicated are shown in Figure 3 (a), (d) and (g), respectively, together with the force-displacement in Figure 3 (b), (e), (h) and force-time responses in Figure 3 (c), (f), (i) for both the experiments and the best fitting model. In our method, a trial set of properties τ_c^α, γ_s, ΔV^α and ΔF^α were determined firstly using prismatic pillar P1 with the mid displacement rate of 0.058 μm/s, and these properties are then employed to predict the responses of (prismatic) pillars P2 and P3 to test the validity of the model across displacement rates of 0.011 μm/s and 0.0008 μm/s, respectively. When the predicted responses of P2 and P3 are not fully consistent with experiments, the properties are incrementally and systematically changed until the final set of properties obtained capture as well as possible all three pillar responses over the three displacement rates. It is noted that ΔV^α and ΔF^α both influence the observed strain rate sensitivity.
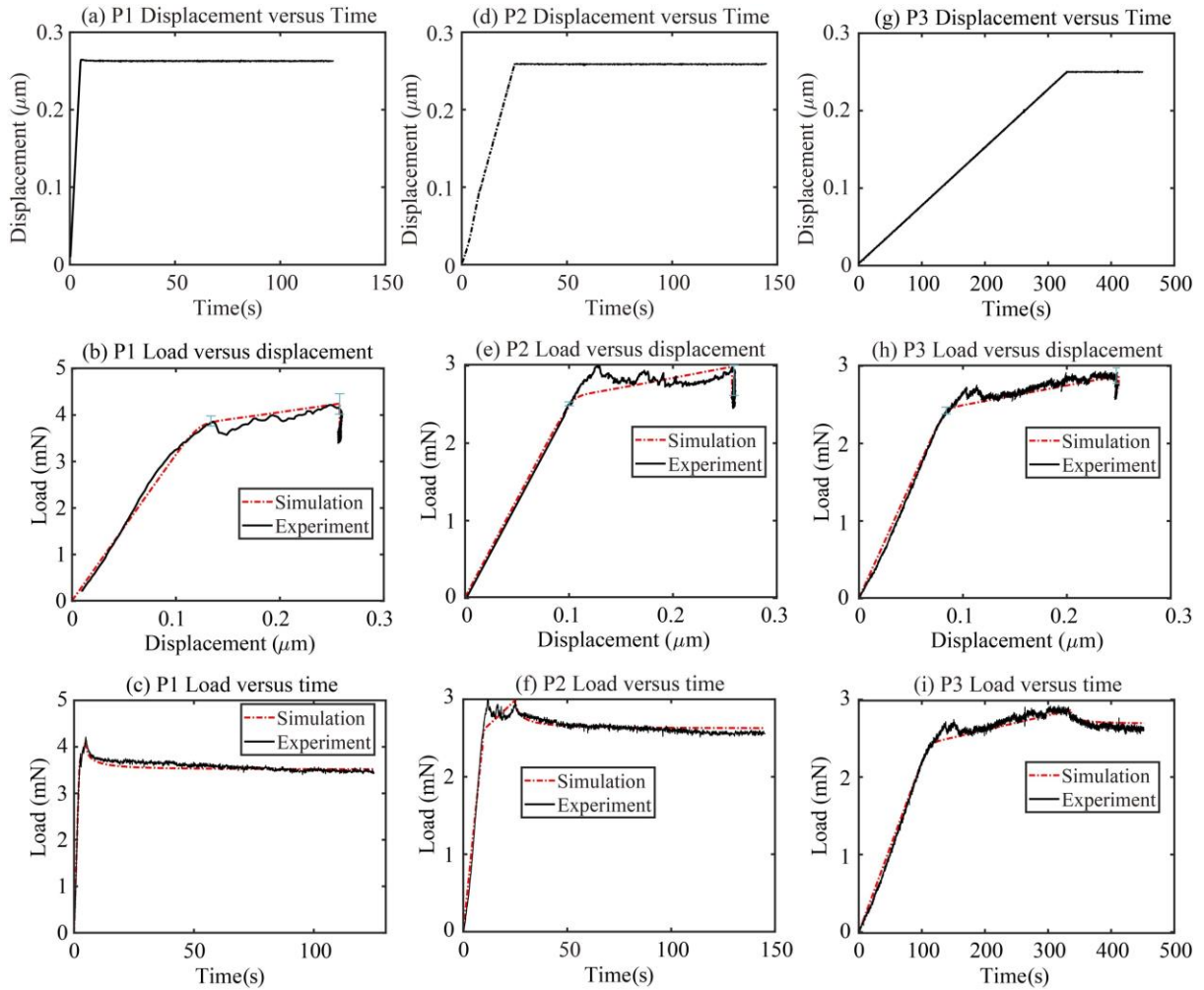
Figure 3 Pillar P1 (a-c), P2 (d-f), P3 (g-i) for prismatic slip in which (a, d, g) shows the applied displacement rates of 0.008 μm/s, 0.058 μm/s and 0.011 μm/s followed by 120 s displacement hold, respectively; (b, e, h) the model and experimental load versus displacement, and (c, f, i) the model and experimental load versus time. Error bars are added at the yielding point and the begin of displacement hold in (b), (e) and (h) for repeated tests.

The same procedure is applied for the basal slip pillars, and the fitting is shown in Figure 4. The anisotropic elastic constants of single crystal Ti and the elastic modulus of the epoxy layer are the same as those used for the prism slip pillars, and are found to give good and consistent representation of the basal pillar experimental data during the elastic load up in Figure 4 (b) and (e). The load increase resulting from the material work hardening is captured using the same hardening coefficient γ_s determined for the prismatic pillars. In Pillar B2, the later part of the load-displacement shows a stress perturbation presumably arising from intragranular defects for dislocations and the associated local hardening. However, the final stress relaxation response observed is similar to that obtained from the pillar model, but starting from a higher initial stress because of the intragranular defects. The complete parameter/property extraction for prismatic and basal slip systems is summarised in Table 2.

It is noted that three or four repeated tests were performed at each displacement rate for prism and basal slip cases and error bars are shown in Figure 3 andFigure 4 to show the variability of yielding and peak forces. The load at yielding point is consistent for each test which gives stable CRSS values. The scatter bars are higher at the beginning of the displacement hold,

likely due to the local dislocation interactions and the rapid stress relaxation which occurs when the displacement hold begins. However, the load drop magnitudes of repeated tests were observed to be stable, which is linked to the strain rate sensitivity of Ti-64 and the key aim of model calibration for obtaining the correct strain-rate sensitive properties, i.e., ΔV^α and ΔF^α.
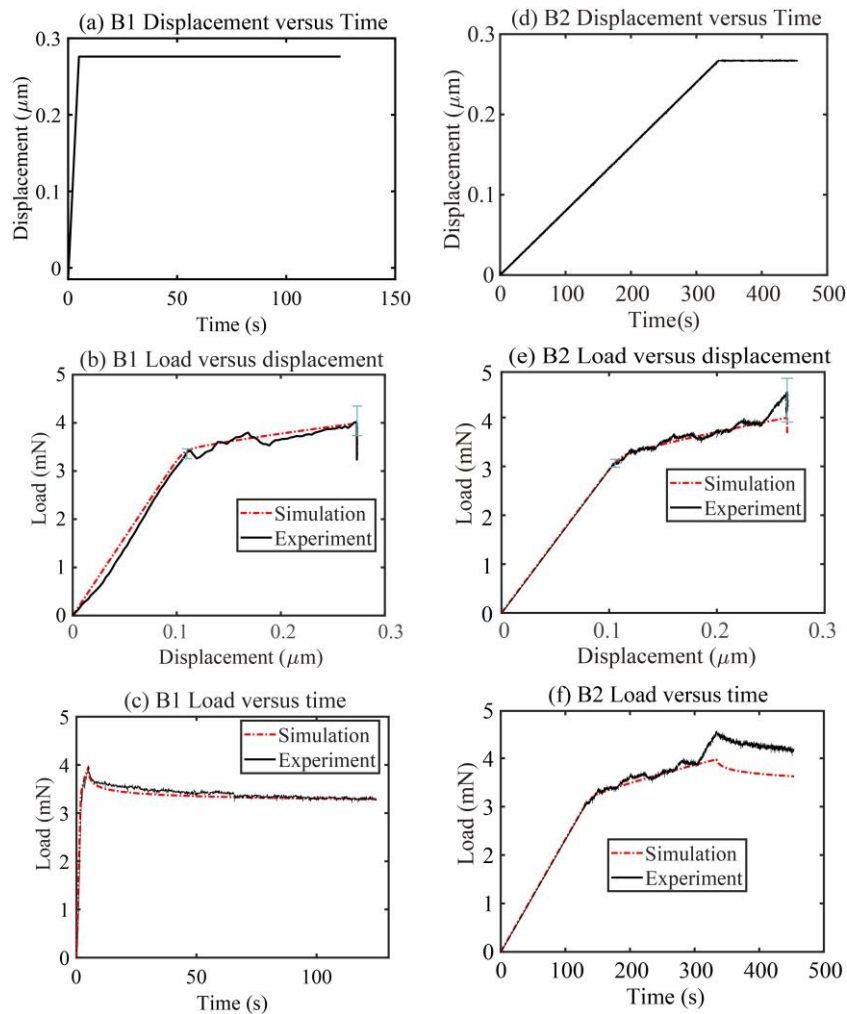

Figure 4. Pillar B1 (a-c) and B2 (d-f) for basal slip in which (a, d) shows the applied displacement rate of 0.0008 μm/s and 0.054 μm/s, respectively, followed by 120 s displacement hold; (b, e) model and experimental load versus displacement, and (c, f) model and experimental load versus time. Error bars are added at the yielding point and the begin of displacement hold in (b) and (e).

The α-phase chemistry in Ti-6Al-4V is different to the chemistry of the alpha phase in Ti-624-x, and this may explain the differences in prism and basal slip [37] strain rate sensitivities. Here, we observe in Ti-6Al-4V that the CRSS for <a> basal slip is 1.13 times the CRSS of prismatic slip. Furthermore, our values are different to prior work where the CRSS values were extracted from macroscopic tests, which were obtained as 325 MPa and 355 MPa for basal and prismatic systems respectively [26]. Hémery and Villechaise calculated an average of the resolved shear stress estimated from the corresponding Schmid factor when the slip traces were found on the specimen surface and this may result in differences, as this macroscopic approach does not consider the local resolved shear stress variations due to equilibrium and compatibility issues within a polycrystal microstructure.

Table 2 Extracted properties of basal and prismatic systems

Parameters at 20 °C		Unit	Basal	Prismatic
Elastic	E_1	MPa	115302	
	E_3	MPa	146100	
	G_{13}	MPa	35419	
	ν_{12}		0.46	
	ν_{13}		0.22	
Plastic	ρ_m	μm^{-2}	5.0	
	ν	Hz	1.0×10^{11}	
	b	μm	2.95×10^{-4}	
	k	$J\cdot K^{-1}$	1.38×10^{-23}	
	γ_s	μm^{-2}	0.05	
	ΔV	μm^3	$19.76\ b^3$	$12.54\ b^3$
	τ_c^α	MPa	393	349
	ΔF	eV	0.60	0.46

The modelling of the pillar compression in order to extract properties has so far not explicitly addressed the possible effects of friction between the punch and pillar. Hence a study has been carried out to investigate representative friction effects between diamond punch and the titanium pillar top surface during loading. For comparison, the case of no friction, low friction, and that for diamond-titanium are assessed particularly in the context of their effects on the resulting pillar force-displacement results which are key to property extraction. The details of these analyses are given in Appendix C where it is shown that the frictional effects are small and could be neglected.

To provide engineering context for the properties obtained, an approximate relationship between conventional instantaneous strain rate sensitivity parameter m^α (ie the gradient of the uniaxial ln[stress] vs ln[strain rate] graph) and the strain rate $\dot{\varepsilon}$ has been derived as [16],

$$m^\alpha = \frac{\partial \ln \sigma}{\partial \ln \dot{\varepsilon}} = \frac{\psi}{\sqrt{1+\psi^2}[\sinh^{-1}\psi + \chi\tau_c^\alpha]} \tag{7}$$

where

$$\psi = \frac{\dot{\varepsilon}}{\xi}; \ \xi = \rho_m \nu b^2 \exp\left(-\frac{\Delta F}{kT}\right)M^\alpha; \ \chi = \frac{\Delta V}{kT} \tag{8}$$

This form is approximate and ignores any role of elasticity, the inhomogeneous deformation which may arise due to single-crystal constraint (e.g. to maintain uniaxial deformation), and dislocation density evolution. However, it can be indicative and the results obtained using the prism and basal slip system properties from pillar tests are shown in Figure 5. Here it can be seen that prism slip is anticipated to have higher strain rate sensitivity than for basal slip over the engineering strain rates ranging from 1.5×10^{-4}/s to 0.01/s. This is consistent with the

recent results on strain rate sensitivity for commercially pure titanium at slightly lower strain rate, which shows higher activation energy ΔV and higher CRSS, together leading to higher strain rate sensitivity in the prism slip system, compared with that in the basal slip system [43].
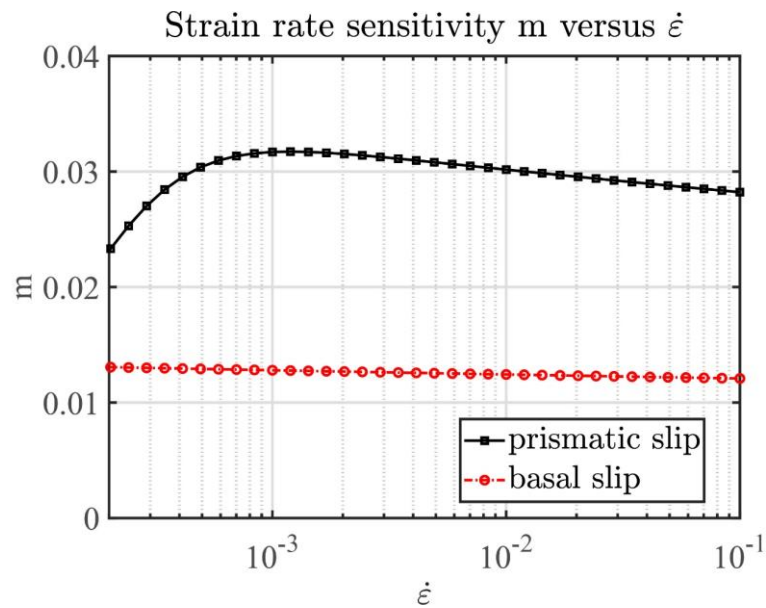

Figure 5 Model predicted strain rate sensitivity, m, anticipated from basal and prismatic slip systems over the strain rate range shown.

4. Dwell fatigue response of characterized Ti-6Al-4V microstructures

4.1 Ti-6Al-4V microstructure characterisation

In order to generate microstructurally faithful models, two Ti-6Al-4V microstructures, representative of forged rotor grade Ti-6Al-4V alloy are used for investigation [35]. These materials had undergone different processing conditions. Representative microstructural images captured using EBSD are shown in Figure 6. The orientation distribution functions (ODFs) are computed and plotted using MTEX-5.1.1 [44] in Figure 6 (b,c). Strong texture is observed in HT1 along X direction and HT2 shows relatively weaker texture and a different texture orientation due to its slightly higher processing temperature.

Both microstructures show strong textures and that the weight-average crystal c-axis directions are distinct in HT1 and HT2 microstructures. Smaller rectangular regions in each microstructure (ROIs) were identified for further study within three-dimensional geometric finite element models where the grain morphologies and crystallographies are set to be the same through the extrusion direction (Z). This has been accomplished through generation of a mesh from the crystal orientation maps extracted from the EBSD data set, and post-processing using MTEX-5.1.1 [44] within MATLAB and also within DREAM-3D-6.4.197 [45]. The grain boundaries were subsequently smoothed, to eliminate the voxelisation resulting from the DREAM.3D representation. The chosen regions are representative of the dominant macro-texture for both microstructures. The mechanical properties of the α-phase are taken from the micro-pillar calibration tests above.
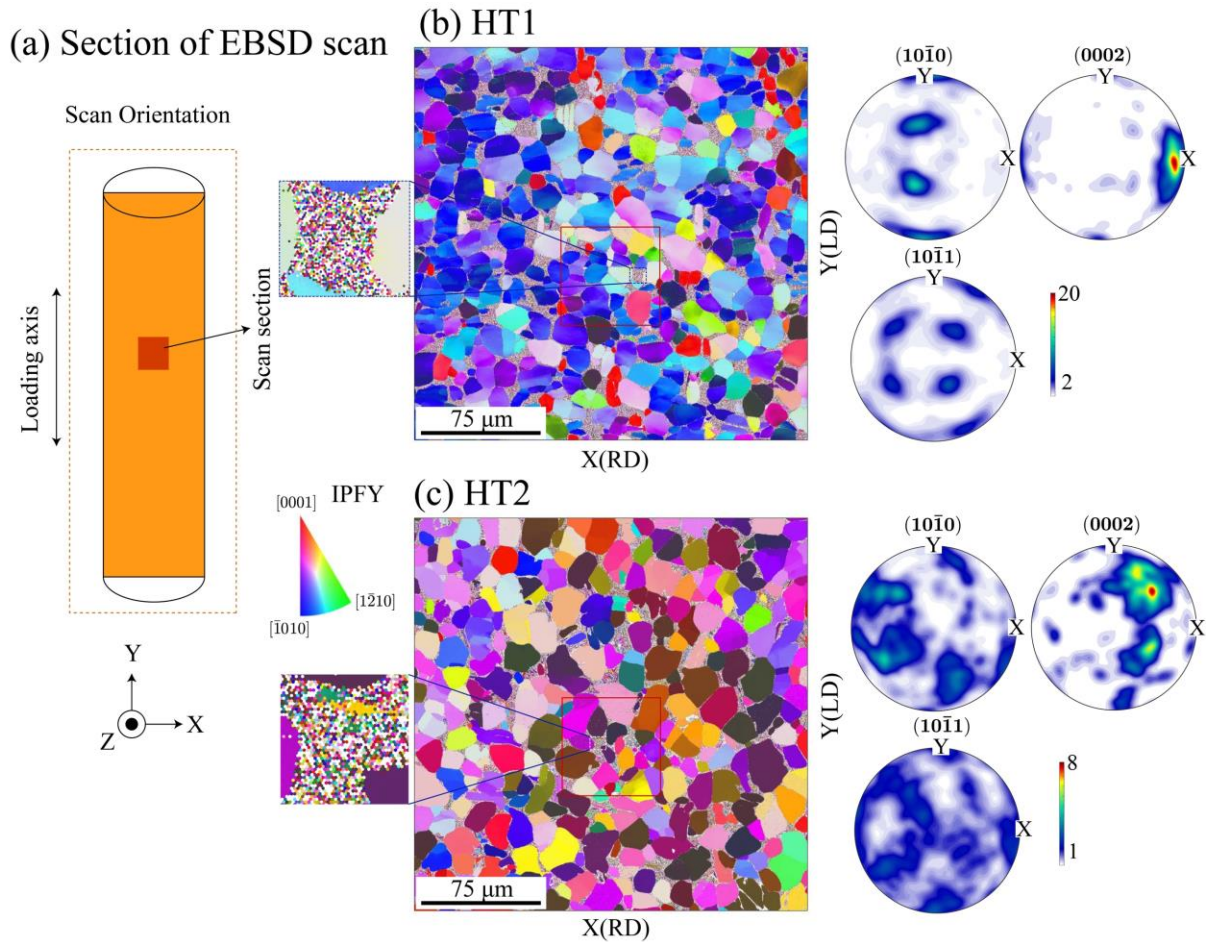
Figure 6 shows schematically (a) the loading direction along Y-axis and the scan section within the sample. The microstructures for the two processing conditions and pole figures of (b) HT1 and (c) HT2 are shown, indicating strong textures and different average c-axis orientations with respect to the loading direction [35]. Subfigures of (b,c) shows the mixed crystallography region where we incorporate the colony structures.

The large scale EBSD map has only been indexed with respect to the α-phase, as the step size and indexing of the β phase made it difficult to resolve this phase. The beta phase can be found within some α-grain regions and typically consists of a transformed beta structure with β-ligaments separating α-laths to form colony structures. To consider the impact of these regions, we introduce them synthetically into the microstructural models and construct representative colony domains. Within these domains, the β phase is assigned an orientation which is generated with respect to the Burgers orientation relationship between the β and α phases. In addition, the inclusion of one or more α-variants is also assessed for our dwell sensitivity predictions described later. In the EBSD scan (Figure 6 (b,c)), the β phase percentage of HT1 (3.3%) is lower than that of HT2 (9.4%). To reflect the differing β phase content, we choose a slightly thicker β lath for HT2 of 1 μm and 0.5 μm for HT1. The spacing is then chosen to reach the appropriate β volume fraction in each microstructure.

The mechanical properties of β have been extracted from Ti-6242 [46] micro-pillar tests and are employed for the β lath structures within the Ti-6Al-4V (with similar chemical composition) here. Examples of local regions of the model microstructures are shown in Figure 7 (a) and (b), indicating the representation of the observed morphologies, the inclusion of β laths, the implementation of the Burger orientation relationship (BOR) between α and β phases, and the inclusion of one or more α variants where appropriate, shown in Figure 7 (c). In the following

modelling, the multi-α-variant case, rather than one single α variant, is chosen for the representation of the local microstructural features.

In the finite element models for both microstructures, the average element size is 2 μm and the element type used is C3D20R with 8 integration points. The model is extruded along the Z direction with 6-element thickness of 6 μm. As shown in Figure 7 (d), U_x of the left edge surface is fixed and U_y of the bottom surface is fixed. U_z at the back surface is fixed. Force or displacement load conditions are applied on the top surface along the Y direction and the appropriate tensile, creep and dwell fatigue loads are introduced as shown in Figure 7 (e), (f) and (g), respectively.

Since we have little information about sub-surface grains, the free-surface grain morphologies and orientations are 3D extruded into the Z-direction. Other studies have shown that though a relatively simple representation of 3D microstructures, this can provide really quite good agreement with experimental DIC surface strain measurements [47]. However, in the case of α−β microstructures, investigations remain to be done to establish how well 2D extruded microstructures can be representative of 3D β morphologies. The absolute Z-direction thickness (3, 6 and 9 μm) and number of elements (2, 4, 6, 8) have been investigated to validate the convergence of surface responses and overall stress-strain responses. A 6 μm absolute thickness was found to be large enough to give no further change to surface responses and the 6-element thickness gave consistent overall tensile stress-strain responses at strain rate of 1×10^{-3}/s.
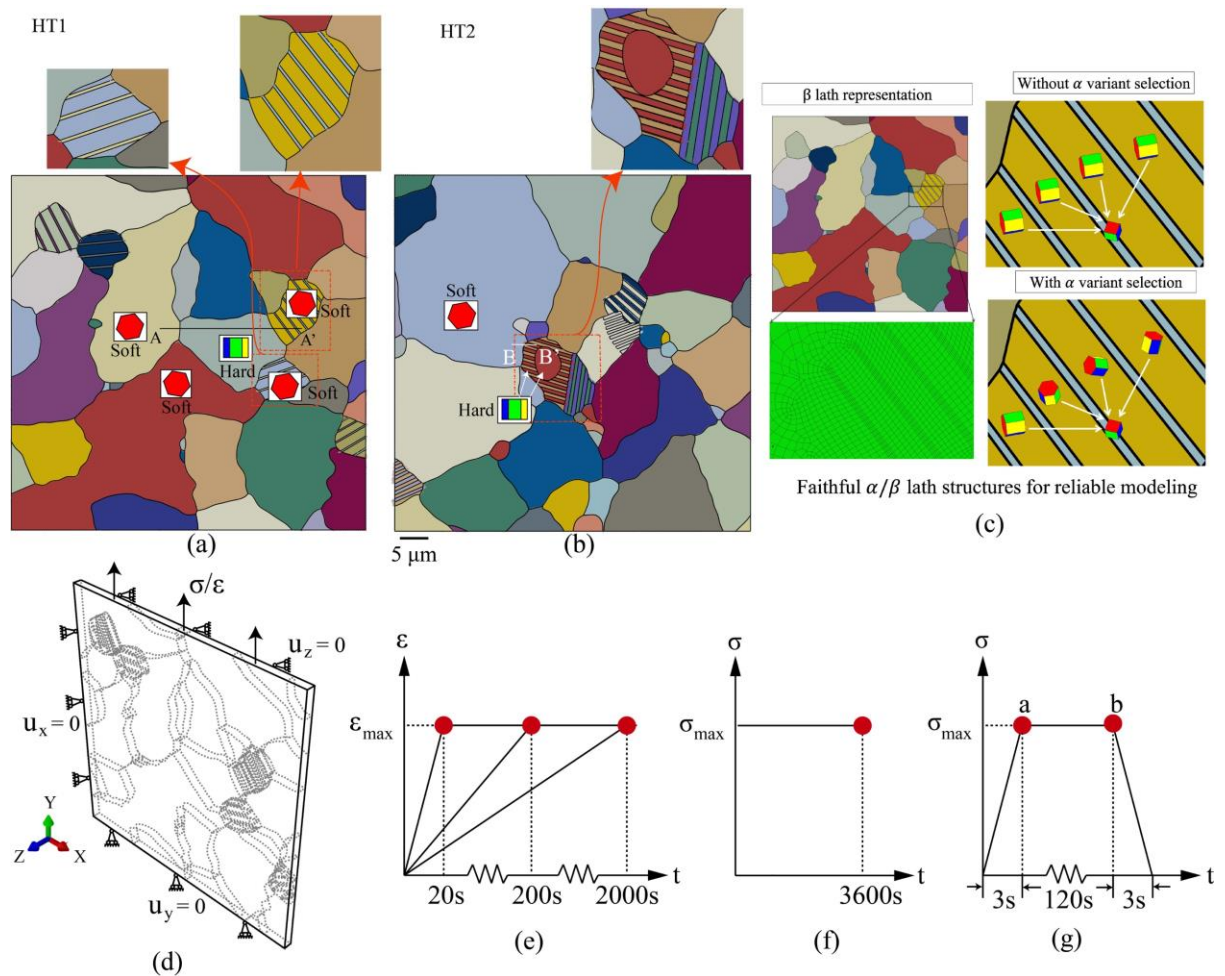

Figure 7 shows (a) the HT1 and (b) HT2 microstructures reconstruction from the EBSD scan [35] with micrographs on top. (c) shows the finite element model representations of the HT1 and HT2 microstructures

including morphology and texture (from EBSD), the inclusion of β laths where where mixed crystallography dots appear in the EBSD scans (shown in subfigures of Figure 6b and 6c), and the inclusion of α variants where required. (d) is the applied boundary condition and loading condition. (e) and (f) are the loading condition for monotonic strain-control tensile test and uniaxial creep test, respectively. (g) represents one cycle under stress-controlled dwell fatigue.

Representative microstructures from HT1 and HT2 have been subjected to uniaxial loading up to a strain of 2% at three strain rates of 1×10^{-2}/s, 1×10^{-3}/s and 1×10^{-4}/s (Figure 7(e)), with a pure α microstructure and inclusion of transformed β domains and example results for HT1 are shown in Figure 8. As anticipated, strong heterogeneity is observed in both quantities as a function of the underlying crystallography, but the average strain is 2% and the average stress approximately 1000 MPa. Despite the low volume fraction of β in HT1 (0.91 %) and HT2 (3.32 %), the β phase in colony grains change local stress and strain distribution significantly. Shown in Figure 8(b,d), the β phase disrupts the slip localisation within the colony grains and leads to higher stresses along the loading direction, which is consistent with previous investigations [20]. Overall, the β phase tends to reduce the strain localisation. This potentially increases the resistance to cold dwell which agrees with recent studies that embedded β within various microstructures, e.g. Widdmansttaten, Basketwave or Colony, leads to reduced load shedding during cold dwell load [20,29].

These models were deformed at three different strain rates, and the predicted average stress-strain responses are shown for both HT1 and HT2 in
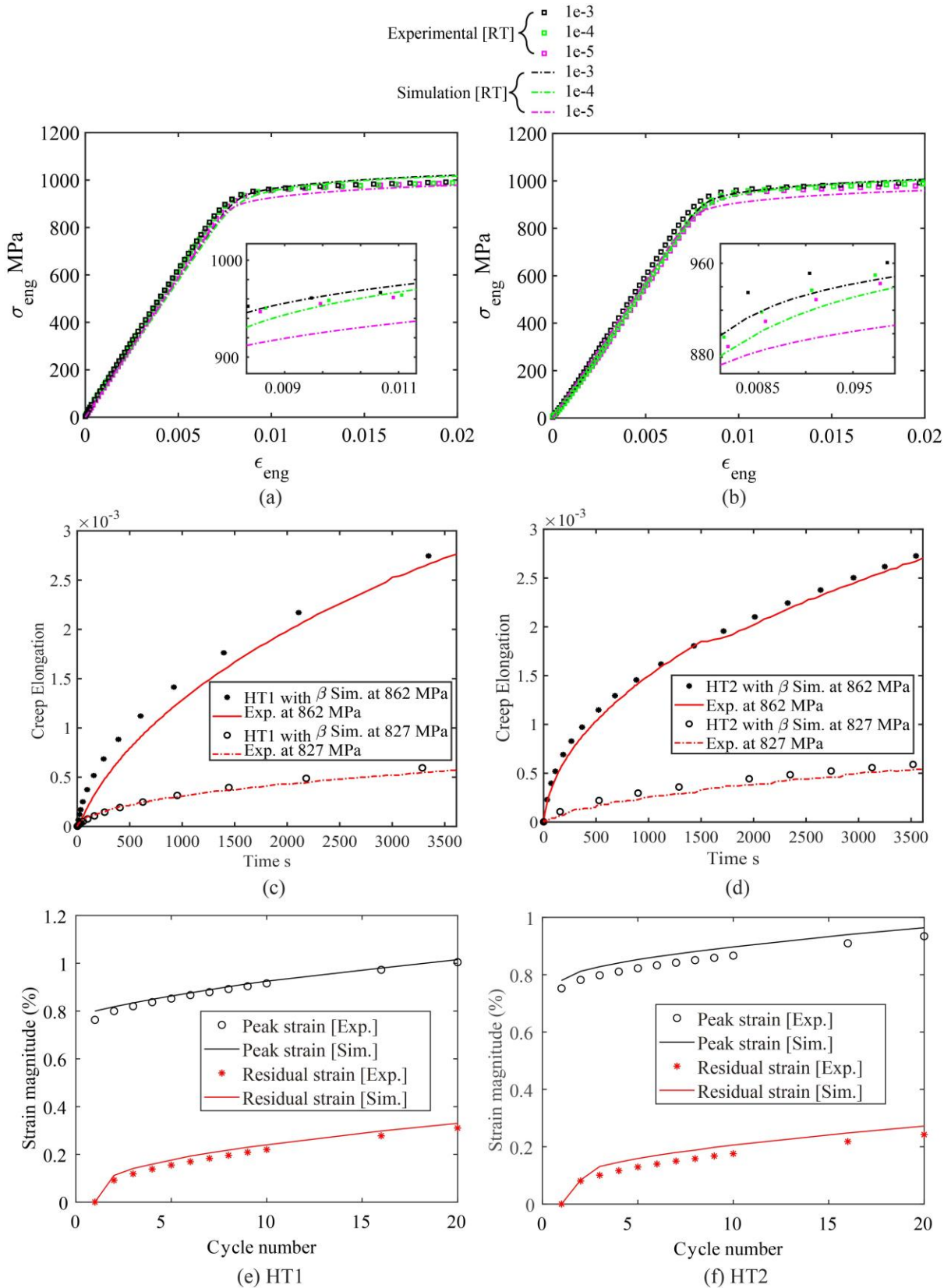
Figure 9, together with good agreement with experimental data [35] (all these tests were performed a room temperature, ~20°C). In addition, the model has been used to predict the creep response of microstructure HT1 subject to stress-controlled loading at 862 MPa and 827 MPa (95% and 90% of yield strength $\sigma_{0.2}$ in Figure 7f), which is also compared with experimental data. The crystallography during tensile and creep modelling remains the same

as the initial grain orientations from EBSD scan. Hence, we have established that the measurement of slip system properties from micro-pillar tests implemented within our crystal slip rule together with faithful α+β microstructures within CPFEM leads to very good capture of independently measured polycrystal stress-strain curves, their macroscopic strain rate sensitivity and their creep responses.

In the context of fatigue loading, the comparisons of polycrystalline strain ratcheting between experimental measurement and simulations have been conducted for HT1 and HT2 for the dwell fatigue loading at 862 MPa (95% of yield strength $\sigma_{0.2}$) shown in Figure 7 (g) in the manuscript using the very same models. The total peak strain at the end of stress hold and the total strain at the cycle start are shown for comparison in
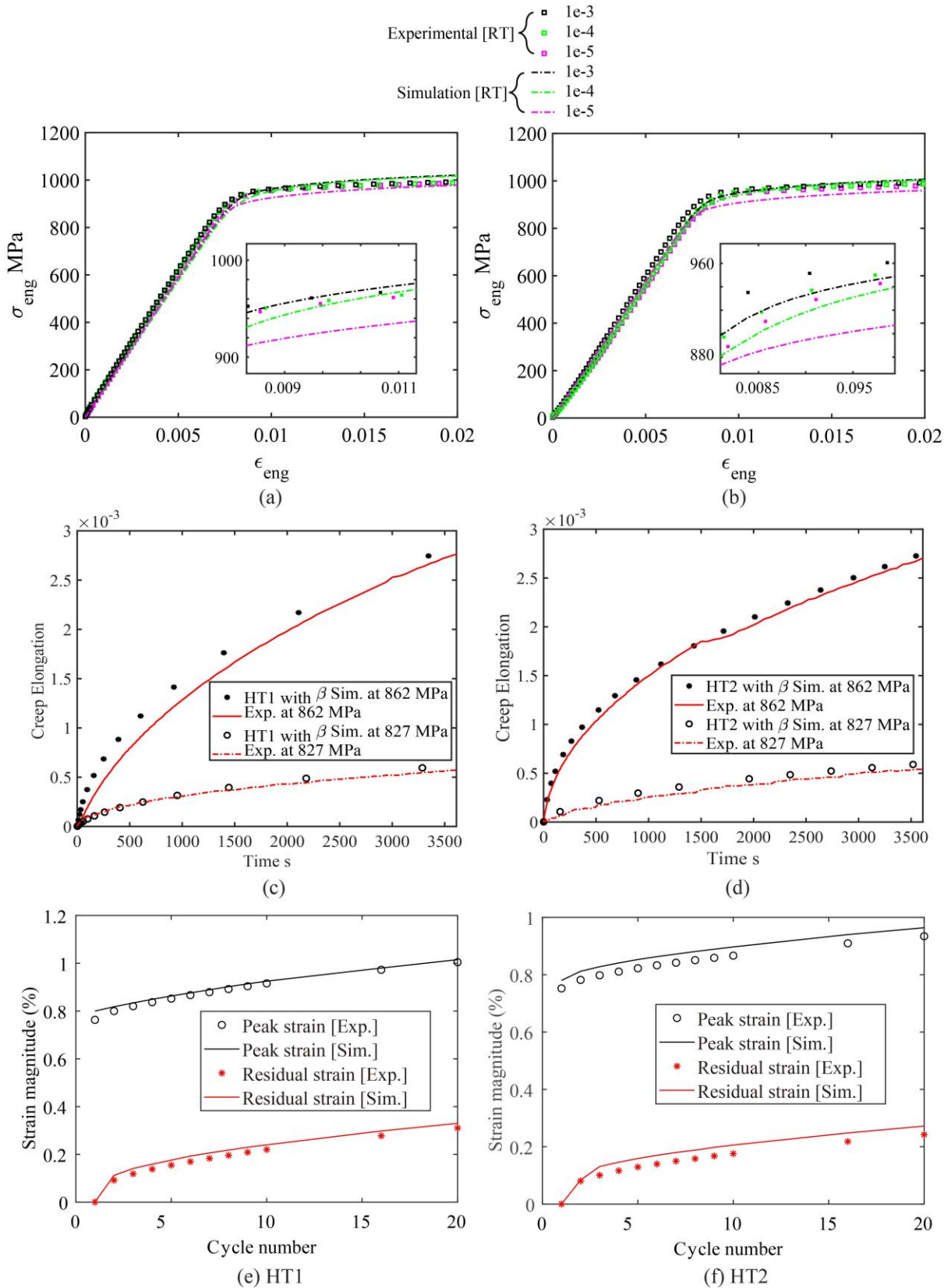
Figure 9 (e,f) for the first 20 cycles. In the modelling, the total strain was computed as the average displacement on the top surface (nodal displacements) divided by the initial model length along the Y-direction. The results show good agreement for cyclic strain ratcheting.
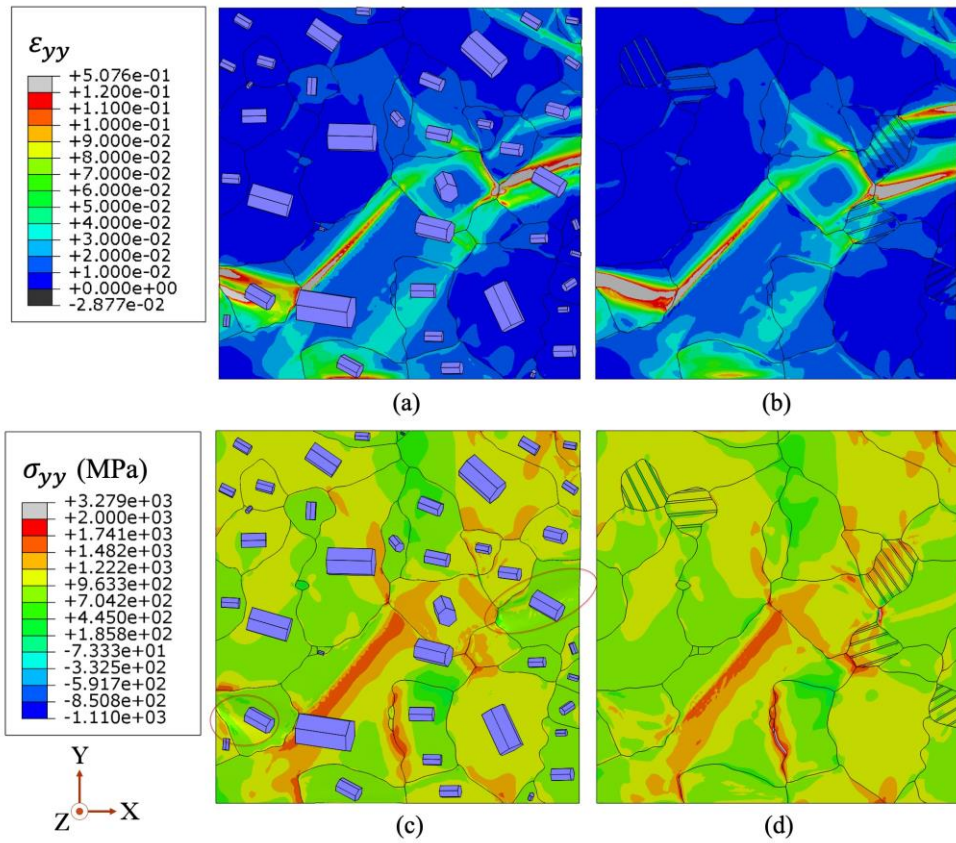
Figure 8 shows the resulting strain and stress distributions after monotonic strain-controlled loading for microstructure HT1 with pure α grains (LHS) (a,c) and including β lath colony regions (RHS) (b,d).
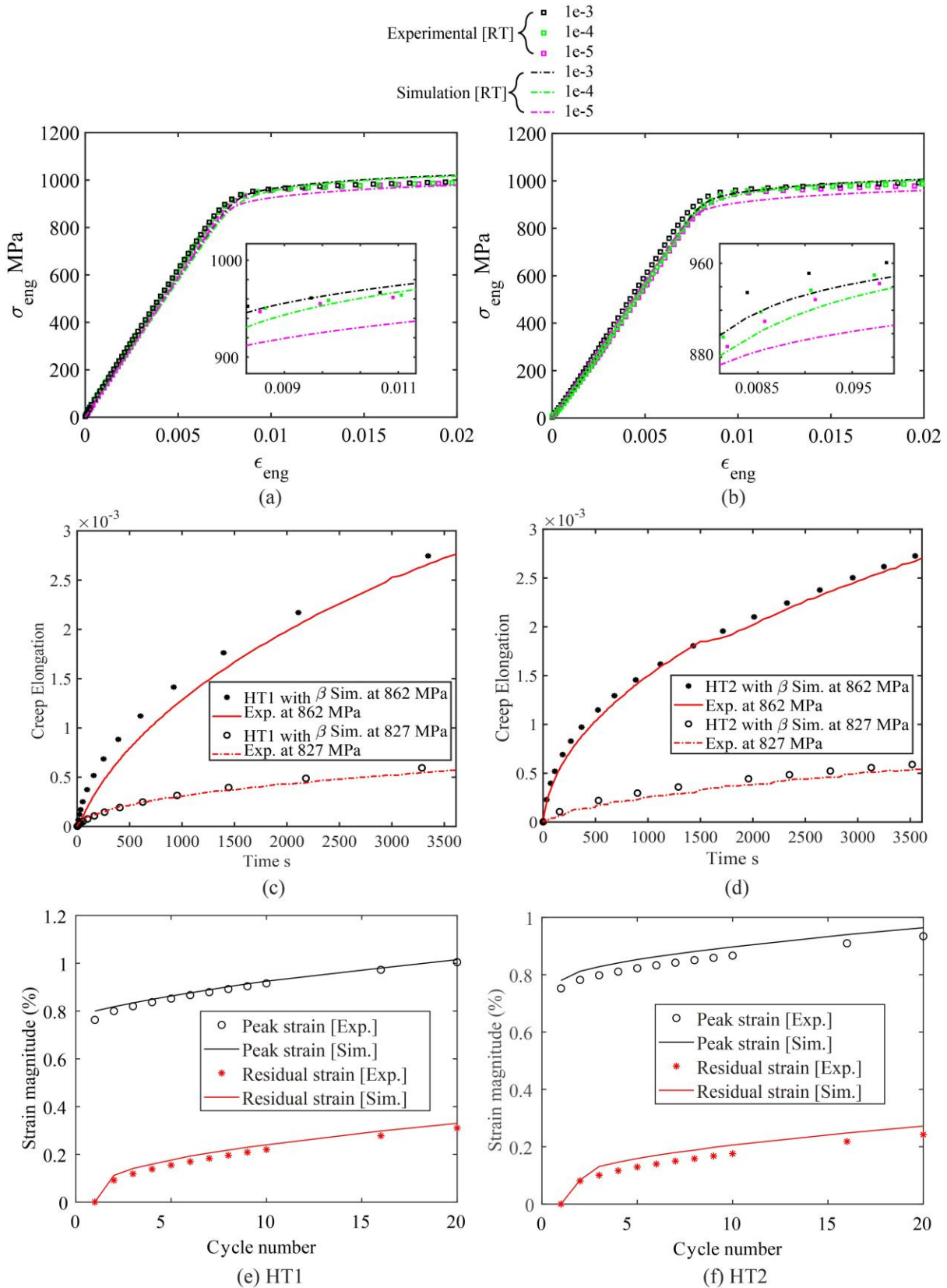
Figure 9 shows the predicted average stress-strain response for the range of strain rates shown for microstructures (a) HT1 and (b) HT2, compared with the experimental data [35]. The predicted creep response of microstructure HT1 subject to stress-controlled loading at 862 MPa and 827 MPa is shown in (c) HT1 and (d) HT2 together with the experimental data. The strain ratcheting of total strain at the end of stress holding (peak strain) and at the cycle start for 20 cycles in (e) HT1 and (f) HT2 microstructures compared with experimental data.

4.2 Microstructural response under dwell fatigue loading

The model established is now used to make predictions of cyclic creep and stress redistribution in two faithfully representative microstructures of the Ti-6Al-4V alloy; and we predict the dwell sensitivity and the S-N life curves for cyclic conditions with and without dwell.

The same two representative microstructures of this alloy labelled HT1 and HT2 shown in Figure 7 (a) and (b) are used. The model was used to simulate dwell fatigue cycles with peak stresses σ_{max} of 862 MPa and 827 MPa (reflecting experimental test stresses at 95% and 90% of yield strength $\sigma_{0.2}$). The fatigue cycle is load controlled to generate a macroscopic stress profile as shown in Figure 7 (g) with a load up and unload time of 3 s and a dwell at peak load of 120 s. To evaluate the 'worst case', a hard-soft grain orientation combination is included in the dwell analysis in the central region. Here we term the hard grain as that with the c-axis parallel to the loading direction such that it does not easily slip, and the soft grain well orientated for slip with c-axis near-normal to remote loading and with rotation of +/-10.5 degree around the c-axis, which triggers most dislocation pile-ups and <a> prism slip activation [48]. During the load hold, it is anticipated that the soft grain will creep and result in load shedding onto the hard grain [7].

Here, the BCC β phase is included where mixed crystallography dots appears in the EBSD scans (shown in subfigures of Figure 6.b and 6.c) and has crystallographic orientation specified which satisfies the Burger Orientation Relationship (BOR) with the adjacent HCP α phase. In this crystal plasticity formulation, slip is transferred into the neighbouring domains due to the requirement that the model must obey compatibility and equilibrium. For colony structures under dwell, the slip in a soft α (colony) grain transfers through the β phase laths, where the latter inhibit but do not eliminate slip transfer such that soft grain creep may occur leading to loading shedding on to the hard grain, and this is supported through detailed understanding using 2D discrete dislocation plasticity analysis by [29]. Two paths, A-A' and B-B' traversing the soft-hard grain pairs, are chosen as shown in Figure 7 (a) and (b) to analyse the load shedding anticipated to take place.

The stress σ_{yy} and strain ε_{yy} distributions developing in HT1 microstructure local configuration near the central hard grain are shown in Figure 10 at points in the loading histories corresponding to the beginning and end of the stress hold during the first applied loading cycle. As hypothesised, regions of high stress are found near the grain boundary but within the hard grain that is next to an α lath within a soft colony region shown in Figure 10 (a.1). These stresses increase significantly during the stress hold in Figure 10 (b.1), due to slip and creep accumulation in the neighbouring soft colony structure and the resulting stress redistribution.
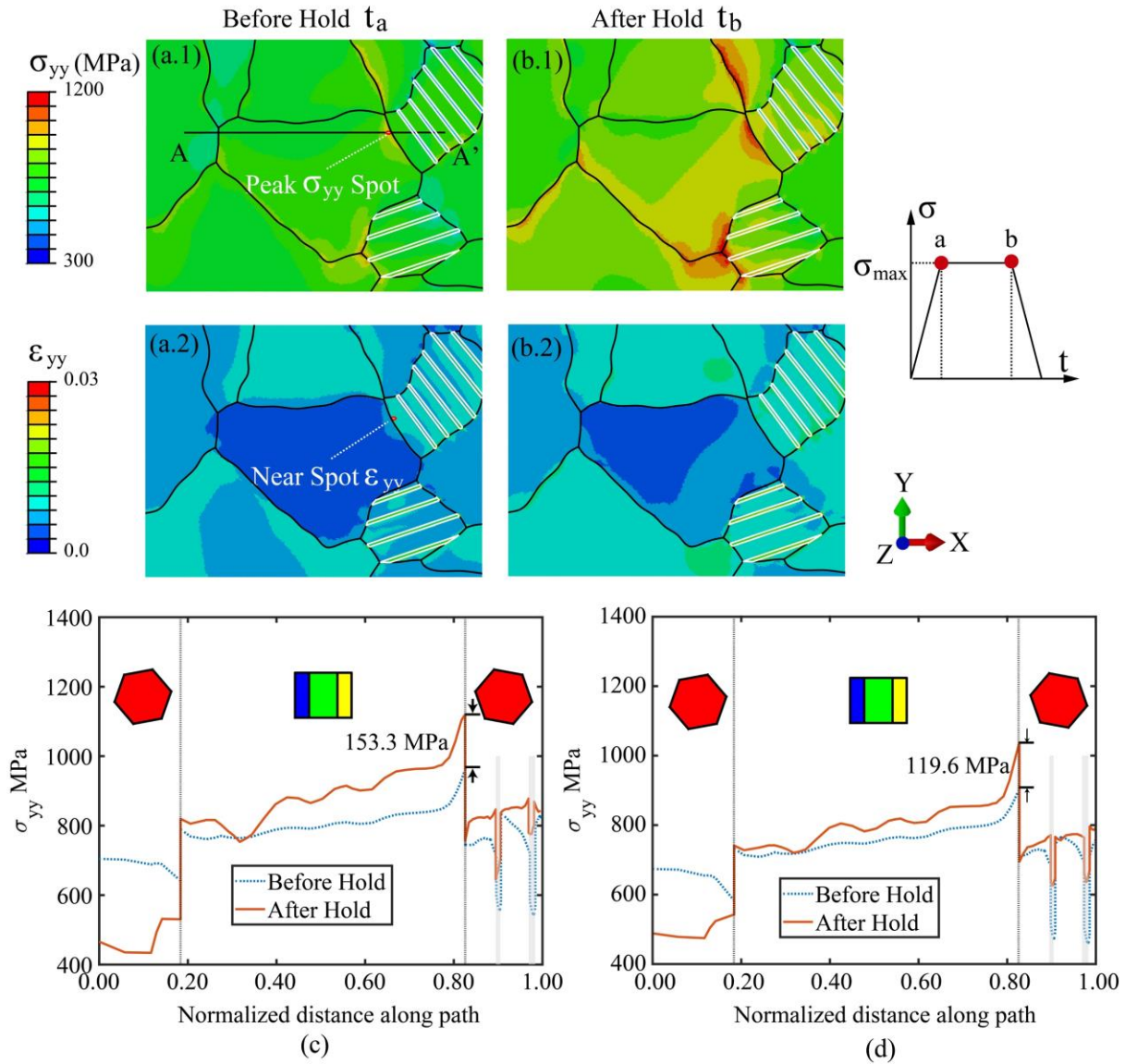
Figure 10 shows stress σ_{yy} and strain ε_{yy} distribution (remote loading along Y-axis) near a central hard grain in HT1 microstructure local configuration at 862 MPa: (a.1) stress distribution before hold at t_a at the red point showing the peak σ_{yy} location (where σ_{yy} is the basal stress inside hard grain); (a.2) total strain distribution before hold at t_a at the red point showing the peak ε_{yy} location; (b.1) stress distribution after hold at t_b; (b.2) strain distribution after hold at t_b. (The white cross-hatch regions are the beta lath structures). σ_{yy} stress distributions along path A-A' are shown in microstructure HT1 for the two differing load levels with peak applied stresses of (c) 862 MPa and (d) 827 MPa, respectively. During the stress hold, the stress redistribution (load shedding) $\Delta\sigma_{yy}$ between t_a and t_b is 153 MPa and 120 MPa, respectively.

The distribution of σ_{yy} stress along path A-A' before and after the stress hold is shown in Figure 10 (a) and (b) for the two dwell fatigue load cycles with peak applied stress levels of 862 and 827 MPa respectively. The σ_{yy} stress increases most at the peak σ_{yy} spot near the grain boundary of the hard grain during the stress hold and the stress component σ_{yy} is the basal stress within the hard grain, important for potential facet nucleation. The stress redistribution (load shedding) $\Delta\sigma_{yy}$ between t_a and t_b for applied stress of 862 MPa is 153.3 MPa at the point indicated in Figure 10 (c). For the lower peak applied stress level of 827 MPa, the local maximum stress level is lower and the stress redistribution (load shedding) is reduced to 119.6 MPa in Figure 10 (d). The (grey) shaded areas in Figure 10 (c-d) within the soft grain indicate the β phase

laths which contribute to the stress changes relating to both the differing β slip strengths and strain rate sensitivities [37].
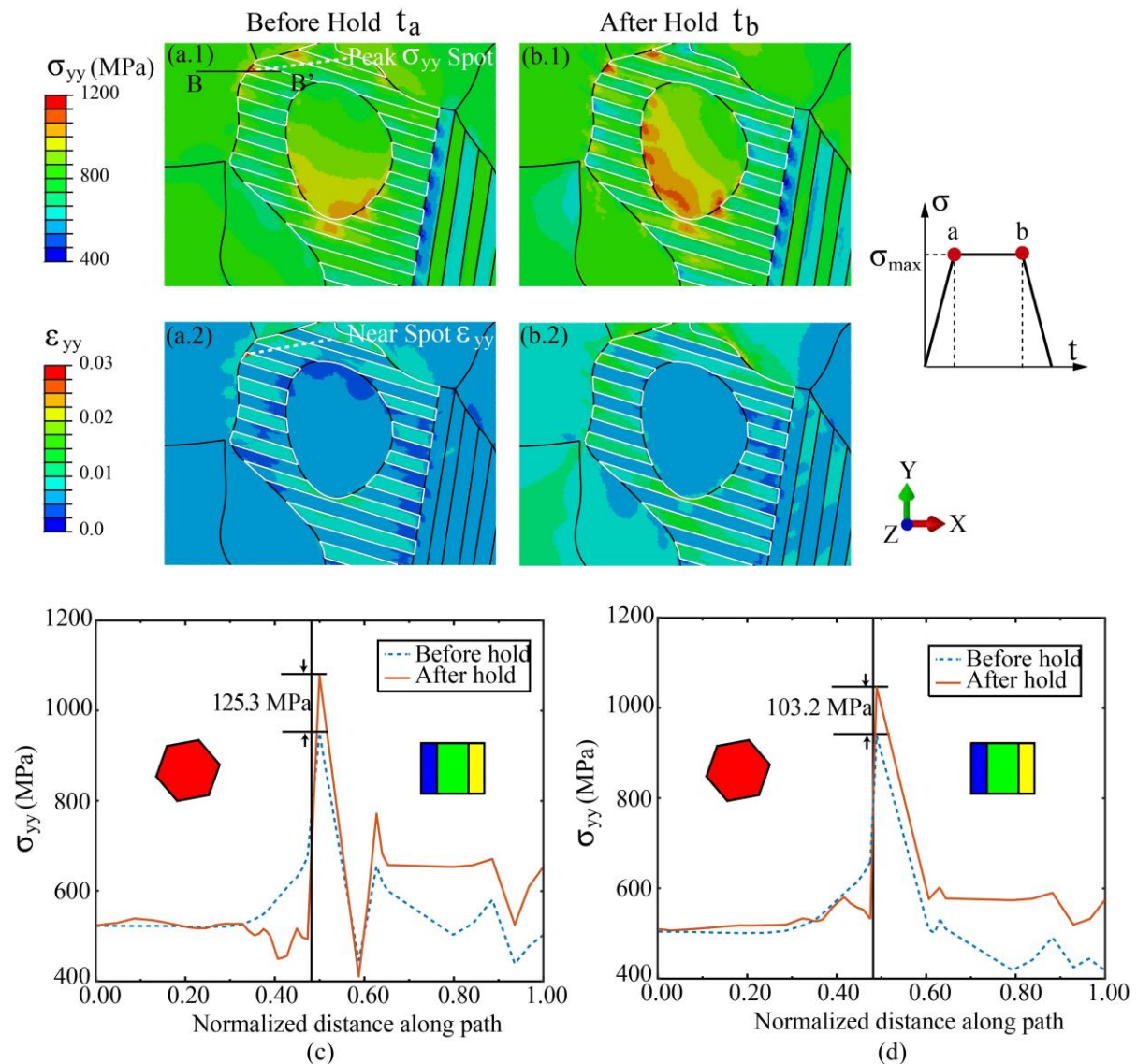

Figure 11 shows the stress σ_{yy} and strain ε_{yy} distributions (remote loading along Y-axis) near the central hard grain of HT2 microstructure local configuration at 862 MPa: (a.1) stress distribution before hold at t_a with red point showing the location of peak σ_{yy} (where σ_{yy} is the basal stress inside hard grain); (a.2) strain distribution before hold at t_a and red point showing location of the peak ε_{22}; (b.1) stress distribution after hold at t_b; (b.2) strain distribution after hold at t_b. (White cross-hatch region is the beta lath structure.) σ_{yy} stress distributions along path A-A' are shown in microstructure HT2 for the two differing load levels with peak applied stresses of (c) 862 MPa and (d) 827 MPa, respectively. During the stress hold, the stress redistribution (load shedding) $\Delta\sigma_{yy}$ between t_a and t_b is 125 MPa and 103 MPa, respectively.

In HT2 microstructure local configuration, the β phase volume fraction is higher with thicker β laths. The central hard grain is embedded in the soft colony structure shown in Figure 11 (a), which has the same orientation as the alpha lath of this colony. The stress concentration is observed at the triple junction of the hard α grain, soft α lath and the β lath and it is enhanced during the stress hold in Figure 11 (b.1). The strain distribution reflects that the local slip in the soft grain increases during the stress hold, again leading to the load shedding.

The stress redistribution in HT2 is reduced compared to that for HT1, mainly due to the width of the β phase laths and the α phase morphological geometry. The increase of β phase width leads to lower volume fraction of α laths and correspondingly reduction of the strain concentration within α laths of the colony structure. Effects of β phase alignment and its crystal orientation have been thoroughly discussed in previous works [29]. Widmanstätten and basketweave morphology with β laths embedded could have significant influence on the local strain rate sensitivity of the microstructure and the load shedding mechanism could be effectively reduced by these effects. The experimentally observed β phase morphology is not entirely clear from the local area of the EBSD scan and a higher resolution scan of the local β phase crystal geometry could result in a better prediction of the local mechanical responses near the grain boundaries between primary α grain and α/β lath structure. A 3D modelling representation of grain structure from sequential EBSD scan using FIB [49] or high energy XRD [8,48] would be beneficial for better representation of 3D grain morphology and crystallography and revealing 3D local grain-scale stress/strain responses under dwell fatigue.

4.3 Microstructure-sensitive dwell and non-dwell fatigue lifetime

The modelling methodology described above is aimed at assessing the dwell characteristics, including sensitivity to dwell fatigue, of differing microstructures which take account of HCP α and BCC β properties obtained from single crystal pillar tests, and explicitly recognising the BOR.

We argue that the dwell sensitivity (including dwell debit) arises from the α-β intrinsic strain rate sensitivities in combination with the constraint effects provided by local microstructural features, where the latter is predominantly combinations of hard/soft grain orientations and colony structures. In fatigue, these lead to progressive cyclic accumulation of slip in the soft grain in turn leading to the cyclic ratcheting up of stress carried by the hard grain. Prior work has indicated that the cyclic rate of accumulation of stress depends crucially on the microstructure (α and β phase properties, phase fractions, morphology and crystallography) as well as the thermo-mechanical loading conditions [51].

In the present work, the crystal plasticity formulation is dislocation based. The evolution of the CRSS includes hardening due to an increase in geometrically necessary dislocation density and thus enables analysis of the impact of local length scale effects. The hardening and progressive load shedding enables the stress on the hard grain to progressively increase. This enables generation of a criterion for facet initiation, and thus component failure, under dwell fatigue. We consider the worst-case normal stress acting on the hard grain achieving a critical value and this critical value can be estimated from the c-axis tensile strength of single crystal titanium ~1200 MPa [52]. In practice, this critical stress value could be modified to take account of alloy chemistry and other effects. But we start with this simple threshold which follows from prior work which evaluated c-axis stresses developing with respect to known facet locations in discs which were assessed by [53]. A cyclic analysis of each polycrystal model is therefore required in order to establish the cyclic rate of stress development at critical points of the microstructure.

From the calibrated crystal plasticity model, these two microstructures are cyclically loaded in this section under dwell fatigue shown in Figure 7 (g). The locations of peak σ_{yy} stress in the hard grain and peak ε_{yy} in the neighbouring soft grain are shown in Figure 10 and Figure 11 for HT1 and HT2 microstructures, respectively. The local peak stress/strain spot shown in Figure 10 and 11 are obtained by computing the average value over a non-local radius region (0.5 μm, 6-8 elements) from values of local integration points. It should be noted that the radius boundary for peak stress does not extend beyond the hard grain, and the same for peak strain not exceeding the soft grain. A clear load shedding behaviour is revealed where stress transfers

from soft grain to hard grain during the load hold. The redistributed stress is relatively lower in HT2 compared with that in HT1 under the same load level, which is mainly affected by the correspondingly lower creep accumulation in the neighbouring soft grain due to lower fraction of α laths.

The peak stress σ_{yy} variations within the central hard grains in both microstructures are computed for 50 cycles for the two loading conditions and shown in Figure 12. The cyclic rate of increase of peak σ_{yy} increases during the first 10 cycles and tends towards a constant rate of evolution after 20 cycles. The strain ε_{yy} at neighbouring soft grains also accumulates at a changing rate in the first 20 cycles but approaches a constant cyclic ratchet rate for higher cycles. Similar behaviour was found for isothermal behaviour in alloy IMI834 leading to facet nucleation. At higher temperatures representative of in-service thermo-mechanical loading conditions, thermal alleviation was shown to lead to a decrease to zero in stress ratcheting thereby eliminating the propensity for dwell fatigue [51]. Similar thermal alleviation is suspected for Ti-6Al-4V and could be predicted under in-service load, which requires crystal-level rate sensitivity data at higher temperatures.
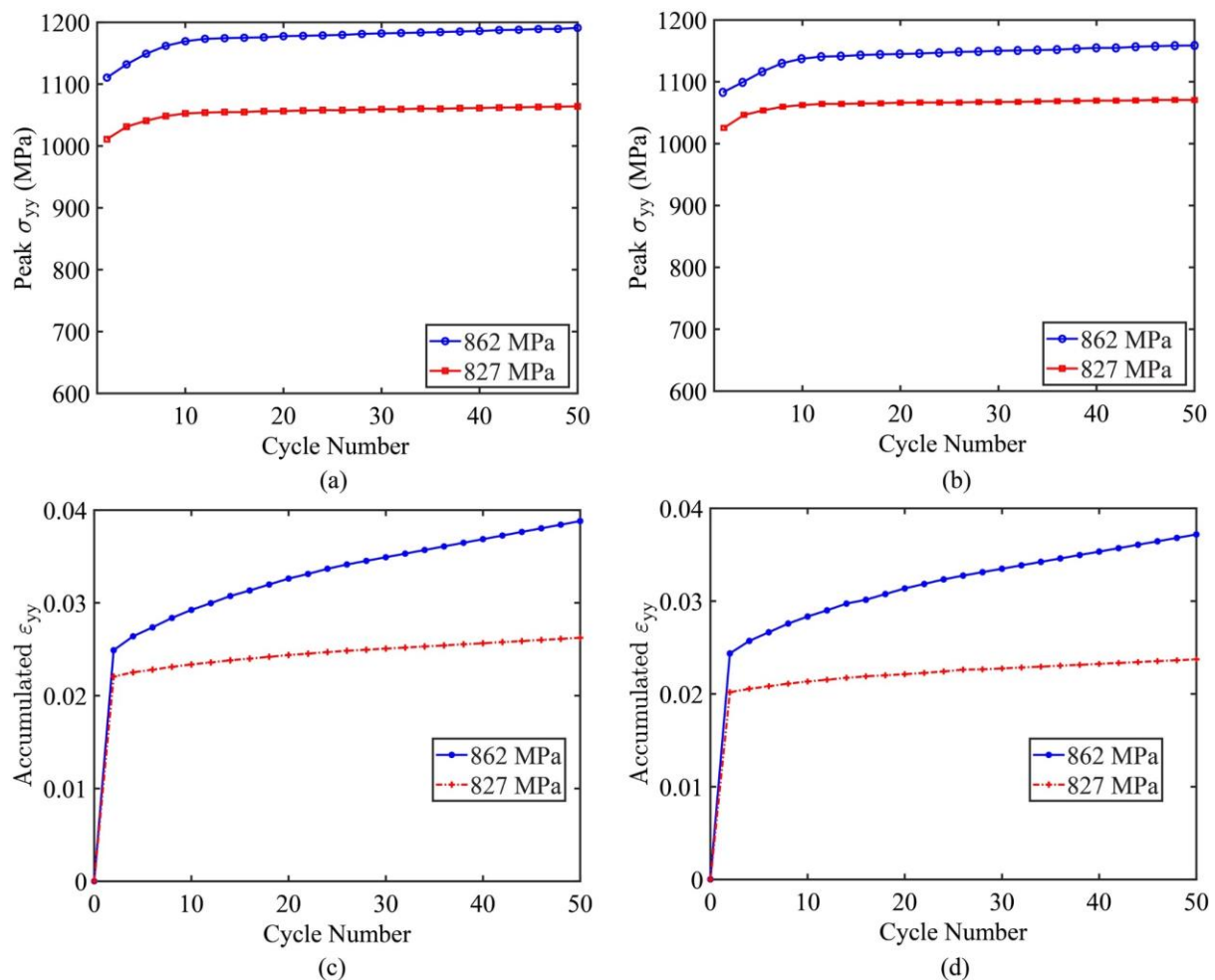

Figure 12 shows maximum stress σ_{yy} at the end of the stress hold for each cycle in the central hard grain for microstructures (a) HT1 and (b) HT2 (corresponding to the hotspots shown in Figure 10 (a.1) and Figure 11 (a.1)) and the ε_{yy} strain accumulation at the end of the stress hold for each cycle in the soft grain (neighbouring the central hard grain) for microstructures (c) HT1 and (d) HT2 (corresponding to the hotspots shown in Figure 10 (b.2) and Figure 11 (b.2))

From the stabilised region of the cyclic ratcheting curves, the peak hard-grain stresses in Figure 12 may be expressed as shown in Table 3 for HT1 and HT2 at two maximum stress levels.

Table 3. Stablised stress σ_{22} accumulation during dwell fatigue cycles

Maximum stress level	HT1 microstructure	HT2 microstructure
862 MPa	$\sigma_{22} = 0.1023N + 1178$	$\sigma_{22} = 0.0839N + 1163$
827 MPa	$\sigma_{22} = 0.0361N + 1058$	$\sigma_{22} = 0.0264N + 1065$

These equations can be used to predict the number of cycles to failure assuming that this occurs for a critical stress level of 1200 MPa [52]. Microstructure HT1 requires 263 and 3985 cycles for applied stress of 862 MPa and 827 MPa, respectively. Microstructure HT2 requires 438 and 5125 cycles, respectively.

This means that we predict that microstructure HT2 to have a higher lifetime to dwell facet nucleation than HT1 for given stress, with the higher volume fraction of the β phase contributing to the alleviation of the strain ratcheting during the stress holds. Our mechanistic understanding derives this response from our observations that the higher maximum applied stress generates considerably higher soft grain creep/cyclic ratcheting giving rise to the one-order decrease of the lifetime.

A similar analysis has been performed for non-dwell fatigue loading condition for HT1 and HT2 to compare with the dwell fatigue lifetime for predicting the dwell debit. In the non-dwell fatigue condition, the load shedding mechanism is reduced. Furthermore, the non-zero mean stress resulting from the load cycle remains sufficient to result in cyclic creep within the soft grain but this is of smaller magnitude, and this leads to a slower accumulation of cyclic stresses on the hard grain at the hard-soft pair.
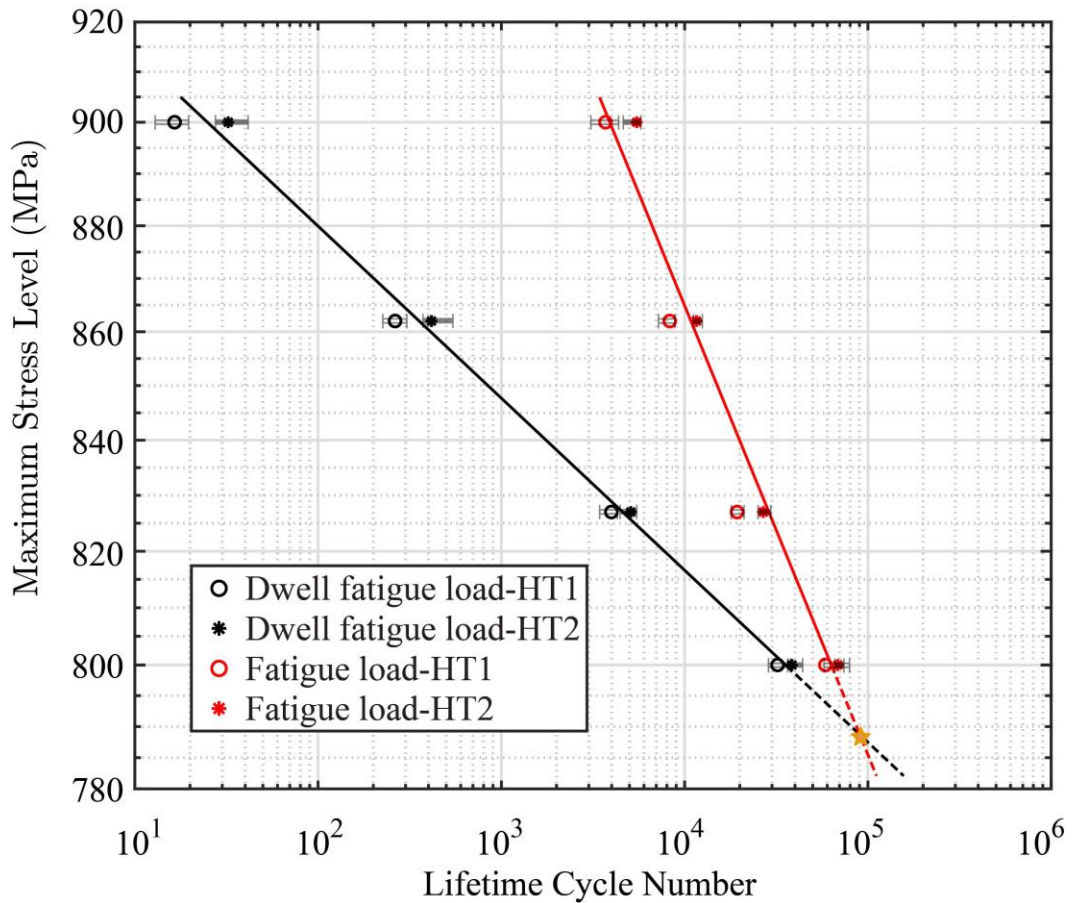
Figure 13 Predicted S-N curves for microstructures HT1 and HT2 under dwell and non-dwell fatigue loading conditions demonstrating the dwell debit in alloy Ti-6Al-4V, assuming a <c> axis normal stress failure criterion of 1200 MPa. Error bars indicate the non-local radius size effect on lifetime predictions.

Figure 13 summarises the model predictions for dwell and non-dwell fatigue for Ti-6Al-4V microstructures HT1 and HT2 for the stresses indicated, and is consistent with the experimental data of [1]. The effect of the non-local radius size used for determination of peak local strres is studied over a range of 0.3 μm to 1 μm (maximum beta width). Corresponding error bars are shown in Figure 13 to quantify the radius effect on non-local peak stress computation and lifetime prediction. A bigger error bar range is observed for higher applied stresses. A linear variation of ln(cycles to failure) with ln(stress) is observed for both dwell and non-dwell loading. As the applied stress level decreases, so the two life curves converge to an applied stress at which the dwell sensitivity would be expected to diminish to zero (i.e. a dwell debit of 1.0). This stress is predicted to be about 790 MPa for the Ti-6Al-4V alloy microstructure considered in this paper under fatigue at 20 ˚C. But this is based on the simple premise that the fracture strength is given by the single crystal Ti c-axis tensile strength. Naturally, experimental fatigue fracture data for alloy Ti-6Al-4V would enable this fracture stress to be refined.

Limitations of the polycrystal model include the pseudo-3D extrusion from 2D EBSD scans instead of a full 3D representation, the uncertainty of α–β colony structure morphology in the EBSD scans such that β phase thickness was chosen to satisfy overall volume fraction data, and of course the limited numbers of grains considered in model microstructures. Despite these limitations, the proposed polycrystal model containing the anisotropic single-crystal properties give reasonable results compared with independent experimental measurements. We urge care when considering this model for in-service predictions, as prior work [51] has indicated that thermal fatigue and alleviation (at ~200 ˚C) can change the impact of the strain rate sensitivity

and accumulation of cyclic stresses. With knowledge of the (commercially sensitive) thermal and loading conditions in a jet engine, we can anticipate that this model is able to help understand creep and cyclic ratcheting, and ultimately the performance of industrial alloys in service.

5. Conclusion

Crystal plasticity slip rule properties for Ti-6Al-4V α phase have been directly extracted from micro-pillar tests at 20 ˚C and used to calibrate slip strength and thermal-activation-based rate sensitivity parameters in the crystal plasticity model. The strain rate sensitivity of prism slip is shown to be somewhat stronger than that for basal slip over the strain rate range considered. The crystal slip rule established for Ti-6Al-4V shows good agreement with the average polycrystal stress-strain and creep behaviour from experimental measurements.

Representative Ti-6Al-4V microstructures have been modelled using the slip properties extracted. Significant stress redistribution from soft to hard crystallographic regions occurs in this material during stress hold (dwell) periods. In addition, cyclic dwell loading leads to progressive creep ratcheting in the soft region resulting in cyclic redistribution of stress on to the hard region, indicating the existence of sensitivity to dwell fatigue and the prognosis of a dwell fatigue debit in this alloy. The local α-β microstructures within the colonies are shown to have quite significant influence on the creep response in crystallographically soft regions.

The dwell fatigue sensitivities of these two microstructures have been quantified. To investigate the worst-case scenario triggering dwell and non-dwell fatigue crack nucleation, a rogue grain combination is embedded in to two differing microstructures analysed. The load shedding and progressive cyclic stress ratcheting for the two microstructures have been calculated. The stress 'ratchet rates' are found to stabilise such that a stress-based criterion has been employed to predict dwell and non-dwell fatigue lives, and the stress below which the dwell debit vanishes (790 MPa) to zero for 20 ˚C loading. The important development for this work is that these fatigue life predictions have been made without any knowledge of experimental fatigue data for the material (i.e. there is no fitting) and are based on the cyclic achievement of a critical stress in the hard grain in a hard-soft grain combination. In this paper, these models have been used to predict fatigue life based upon the c-axis tensile strength for α-Ti, but the true fracture strength for Ti-6Al-4Vcould be established by experiment to improve dwell fatigue life predictions.

Acknowledgements

Appendix A. Frame compliance

In pillar compression testing, the pillar forms part of a load train which includes the loading column, the punch, the pillar, the pillar base with the same crystal orientation as the pillar, and the base substrate (epoxy glue). A detailed presentation of assessment of the compliance and extraction of pillar displacement is given in [37], and a summary is given here. The total displacement is divided into the following contributions labelled punch, base, substrate beneath the base and pillar,

$$u_{\text{tot}} = u_{\text{punch}} + u_{\text{base}} + u_{\text{substrate}} + u_{\text{pillar}} \qquad (A.1)$$

The force is considered identical along this load train [37] and compliance of the rig is decomposed into frame and pillar, which are then decomposed further as

$$\frac{1}{k_{\text{tot}}} = \frac{1}{k_{\text{frame}}} + \frac{1}{k_{\text{pillar}}} = \frac{1}{k_{\text{punch}}} + \frac{1}{k_{\text{base}}} + \frac{1}{k_{\text{substrate}}} + \frac{1}{k_{\text{pillar}}} \qquad (A.2)$$

The modelling of the pillar (indicated in Figure 2(a)) explicitly includes the pillar, the base (with the same crystallographic orientation as the pillar) and the (epoxy) glue. The glue substrate is subject to Z-direction constraint on its bottom surface and a single point constraint in both X and Y directions at the bottom-center of the glue layer. Its Poisson's ratio is given as 0.3 [42] and is now provided. As mentioned in Section 3, the elastic modulus of the isotropic substrate made from cyanoacrylate based (epoxy) glue was found to be 9.1 GPa [32] within the manufacturer's range of 3-15 GPa [42] such that it is compliant with respect to other parts of the load train. The modulus of the diamond punch is about 1050 GPa, and that of the steel loading column is ~240GPa which contributes little (~ 3%) to frame compliance. From the pillar study in Section 3, recognising that the pillar and its base are of the same crystallographic orientation (and therefore different for the prism and basal pillars), it is important that the anisotropic elasticity arising in the two cases is fully represented in the modelling to ensure the stiffness differences between the basal and prism pillars are captured. The effective Young's modulus of the titanium base is of order 120 GPa (only for the purposes of this discussion) and its compliance is therefore about 10 times lower than that of the substrate. Hence, the frame compliance of about 0.12 GPa^{-1} is largely dominated by the substrate. The difference in crystallographic orientation of the titanium base (from prism to basal pillars) leads to ~5% variation in load train compliance. Accurate estimation of frame compliance is necessary, as discussed in relation to Figure 2, for capturing the pillar compression (displacement) response. But it is not relevant to slip strength extraction. Ignoring the effect of the substrate would leads to overestimation of the displacement speed or strain rate and larger strain magnitude during relaxation stage.

Appendix B. Model mesh convergence and slip trace analysis

Convergence (mesh) studies have been done before the property extraction process. The volume area of the pillar base maintains consistent mesh density with the pillar. Figure A1 shows that stress convergence (within 2% stress level) is reached with the pillar containing over 750 elements. In the actual model, we use 3000 elements to give a better understanding of local stress/strain responses.

The comparison between computed strain distributions and deformation in pillars is shown in Figure A2 corresponding to the end of loading. Here, the slip traces are shown on the front and back surfaces of the pillars reflected by the strain localisation in the model on these surfaces. Naturally the CP analysis does not capture the full discreteness of the slip trace observations in the single crystal experiments.

Regarding the strain localisation, 5% total engineering strain (displacement divided by pillar height) is applied to the pillars, leading to local effective plastic strain levels up to 0.25.

Compared with basal pillars, more significant strain localisation is observed in the prism pillars, which is shown as discrete slip traces in the experiments. This discreteness leads to experimental force fluctuation at the onset of slip and the strain hardening stages. For the slip strength extraction, the resolved shear stress can be extracted from the modelled force-displacement curves. The flat punch has full contact with the top surface of the pillar during the load-up and force relaxation stages both in the model and the experiment.
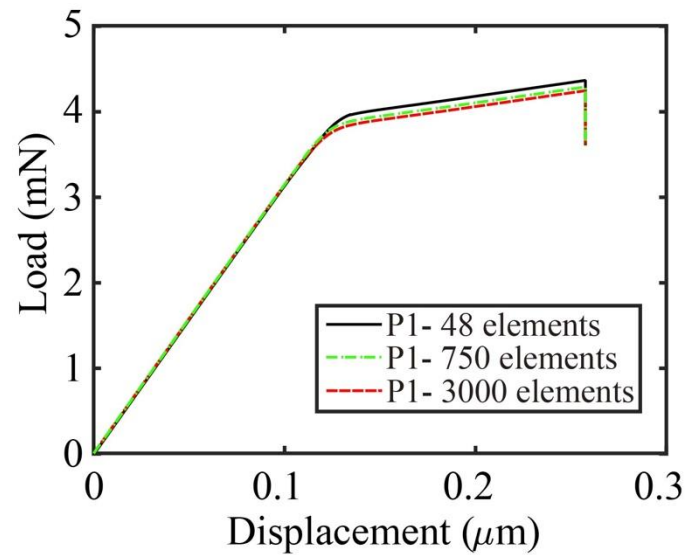

Figure A1 shows mesh convergence study for different element numbers within pillar only for P1.

(a) Basal - Front   (b) Basal - Back
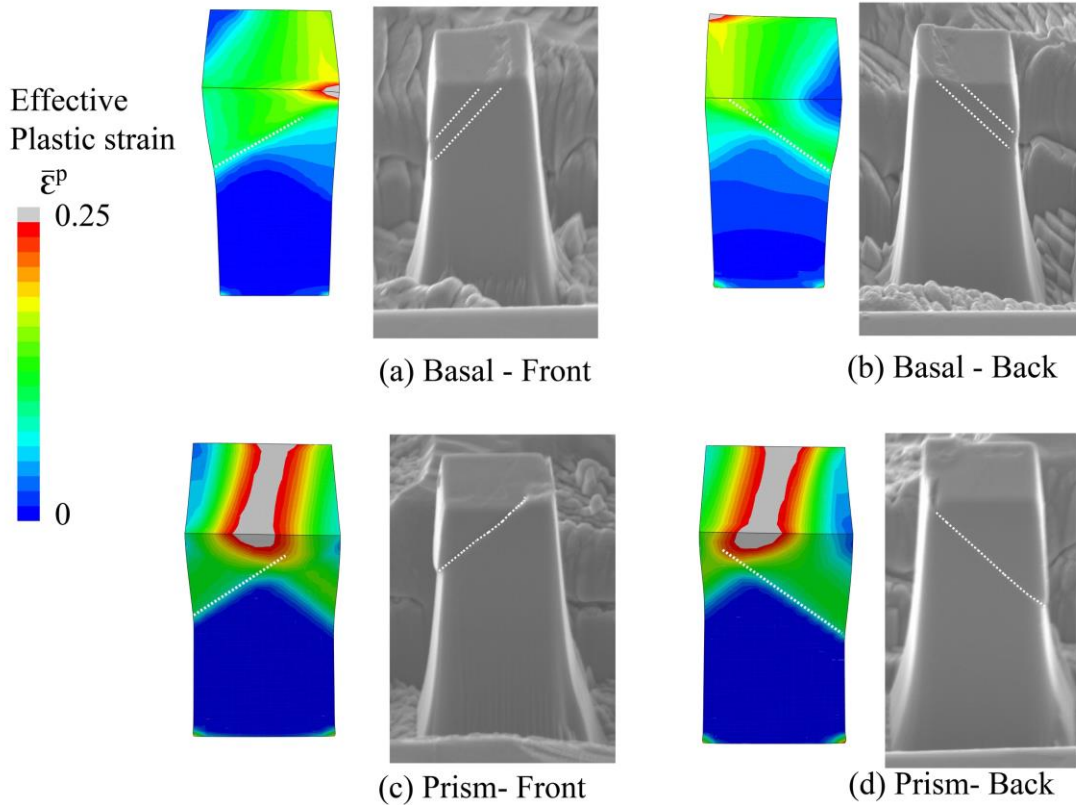
(c) Prism- Front   (d) Prism- Back

Figure A2 shows effective plastic strain distribution compared with slip traces observed in the experiment for both prism and basal pillars at the end of loading.

Appendix C. Punch/pillar friction effect

The pillar compression modelling has been extended to include explicitly the punch (loading the pillar) and the potential frictional effects at the punch/pillar interface, as shown in Figure A3. The top middle of the pillar is aligned with the bottom tip of the punch in Figure A3 (a) and the punch with tip of 20 μm diameter (much larger than pillar width of 3 μm) is shown in Figure A3 (b). The contact between punch and pillar is considered solely as an isotropic tangential contact behavior. The stabilised contact friction coefficient after initial sliding in tribology testing with diamond-coated titanium against titanium is reported as 0.1 [54], which is chosen as the contact friction coefficient in the modelling. A comparative test with low friction coefficient of 0.001 is also carried out. The mesh refinement of the punch tip is set the same as that of the pillar top to avoid contact convergence issue in finite element analysis.

The local deformation comparison between Diamond-Ti contact and a low friction contact are given in Figure A4. It shows that there are some differences in the displacements observed (particularly for the z-direction near the interface), but with limited impact on the slip trace identification since the slip/deformation localisation band direction does not change. In relation to the material property extraction, the load-displacement calculations from the model are shown for the three cases of no explicit punch (reflecting the results in the paper), and the two friction coefficients, in Figure A5. This indicates that the incorporation of the punch/pillar

frictional interface has little impact on the material properties extracted from the force-displacement curves.
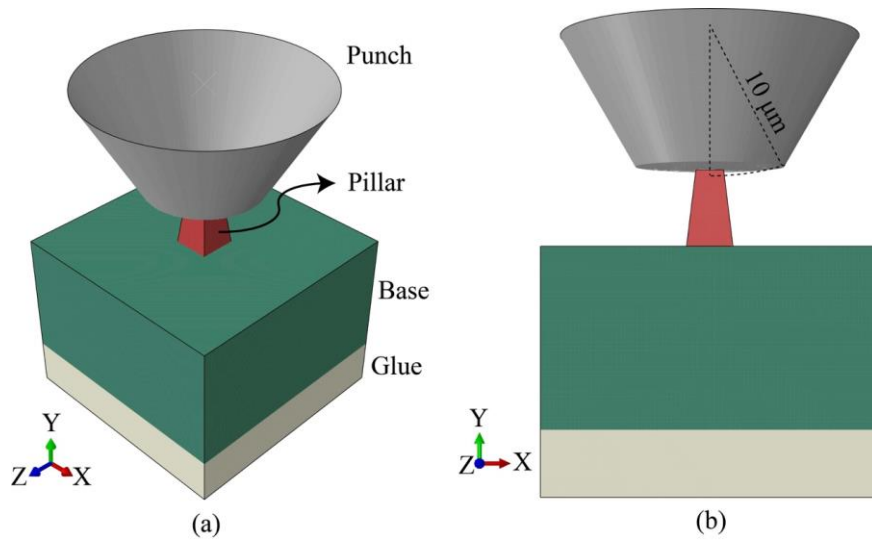

Figure A3 A contact incorporated model with punch on top of the pillar in (a) 3D view and (b) Z-direction view.
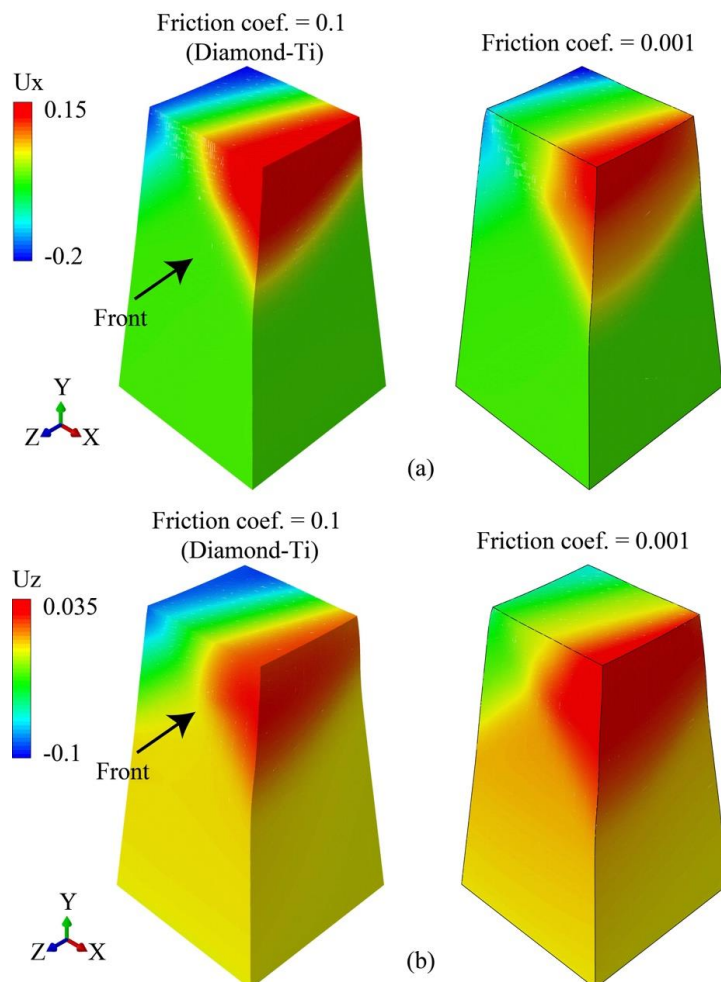

Figure A4 Local deformation comparison of (a) Ux and (b) Uz for P1 pillar for punch/pillar friction coefficients of 0.1and 0.001.
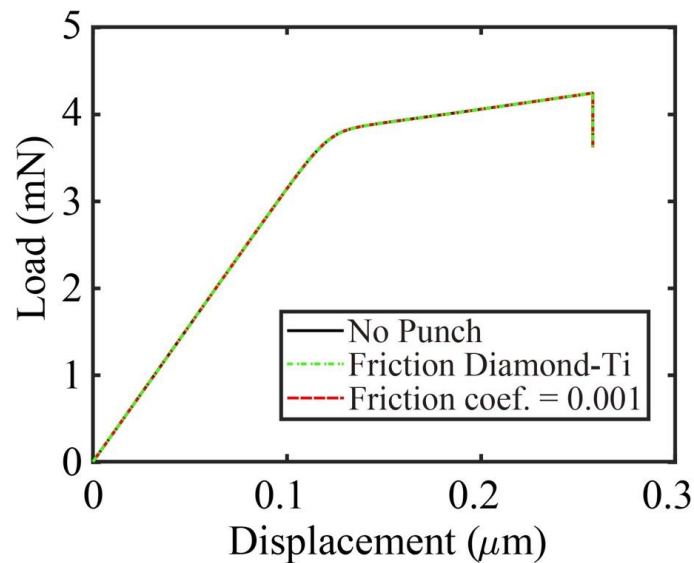
Figure A5 Modelled force-displacement curves for pillar analyses for the cases of no explicit punch, and for punch/pillar friction coefficients shown.

Reference:

[1]   M.R. Bache, A review of dwell sensitive fatigue in titanium alloys: The role of microstructure, texture and operating conditions, Int. J. Fatigue. 25 (2003) 1079–1087. doi:10.1016/S0142-1123(03)00145-2.

[2]   Z. Song, D.W. Hoeppner, Size effect on the fatigue behaviour of IMI 829 titanium alloy under dwell conditions, Int. J. Fatigue. 11 (1989) 85–90. doi:10.1016/0142-1123(89)90002-9.

[3]   M.R. Bache, M. Cope, H.M. Davies, W.J. Evans, G. Harrison, Dwell sensitive fatigue in a near alpha titanium alloy at ambient temperature, Int. J. Fatigue. 19 (1997) 83–88. doi:10.1016/s0142-1123(97)00020-0.

[4]   D. Ozturk, A.L. Pilchak, S. Ghosh, Experimentally validated dwell and cyclic fatigue crack nucleation model for α–titanium alloys, Scr. Mater. 127 (2017) 15–18. doi:10.1016/j.scriptamat.2016.08.031.

[5]   V. Sinha, M.J. Mills, J.C. Williams, Crystallography of fracture facets in a near-alpha titanium alloy, Metall. Mater. Trans. A. 37 (2006) 2015–2026. doi:10.1007/s11661-006-0144-5.

[6]   V. Hasija, S. Ghosh, M.J. Mills, D.S. Joseph, Deformation and creep modeling in polycrystalline Ti-6Al alloys, Acta Mater. 51 (2003) 4533–4549. doi:10.1016/S1359-6454(03)00289-1.

[7]   Z. Zheng, D.S. Balint, F.P.E. Dunne, Rate sensitivity in discrete dislocation plasticity in hexagonal close-packed crystals, Acta Mater. 107 (2016) 17–26. doi:10.1016/j.actamat.2016.01.035.

[8]   K. Chatterjee, J.Y.P. Ko, J.T. Weiss, H.T. Philipp, J. Becker, P. Purohit, S.M. Gruner, A.J. Beaudoin, Study of residual stresses in Ti-7Al using theory and experiments, J. Mech. Phys. Solids. 109 (2017) 95–116. doi:10.1016/j.jmps.2017.08.008.

[9]   S. Huang, D.W. Brown, B. Clausen, Z. Teng, Y. Gao, P.K. Liaw, In situ neutron-diffraction studies on the creep behavior of a ferritic superalloy, Metall. Mater. Trans. A Phys. Metall. Mater. Sci. 43 (2012) 1497–1508. doi:10.1007/s11661-011-0979-2.

[10]   V. Sinha, M.J. Mills, J.C. Williams, Determination of crystallographic orientation of dwell-fatigue fracture facets in Ti-6242 alloy, J. Mater. Sci. 42 (2007) 8334–8341. doi:10.1007/s10853-006-0252-z.

[11]   F.P.E. Dunne, A. Walker, D. Rugg, A systematic study of hcp crystal orientation and morphology effects in polycrystal deformation and fatigue, Proc. R. Soc. A Math. Phys. Eng. Sci. 463 (2007) 1467–1489. doi:10.1098/rspa.2007.1833.

[12]   S. Ghosh, P. Chakraborty, Microstructure and load sensitive fatigue crack nucleation in Ti-6242 using accelerated crystal plasticity FEM simulations, Int. J. Fatigue. 48 (2013) 231–246. doi:10.1016/j.ijfatigue.2012.10.022.

[13]   G. Venkataramani, K. Kirane, S. Ghosh, Microstructural parameters affecting creep induced load shedding in Ti-6242 by a size dependent crystal plasticity FE model, Int. J. Plast. 24 (2008) 428–454. doi:10.1016/j.ijplas.2007.05.001.

[14]   S. Joseph, T.C. Lindley, D. Dye, Dislocation interactions and crack nucleation in a fatigued near-Alpha titanium alloy, Int. J. Plast. 110 (2018) 38–56. doi:10.1016/j.ijplas.2018.06.009.

[15]   Z. Zheng, S. Waheed, D.S. Balint, F.P.E. Dunne, Slip transfer across phase boundaries in dual phase titanium alloys and the effect on strain rate sensitivity, Int. J. Plast. 104 (2018) 23–38. doi:10.1016/j.ijplas.2018.01.011.

[16]   Z. Zhang, F.P.E.E. Dunne, Microstructural heterogeneity in rate-dependent plasticity of multiphase titanium alloys, J. Mech. Phys. Solids. 103 (2017) 199–220. doi:10.1016/j.jmps.2017.03.012.

[17]   W.H. Miller, R.T. Chen, E.A. Starke, MICROSTRUCTURE, CREEP, AND TENSILE DEFORMATION IN Ti-6Al-2Nb-1Ta-0. 8Mo., Metall. Trans. A, Phys. Metall. Mater. Sci. 18 A (1987) 1451–1467. doi:10.1007/bf02646658.

[18]   S. Suri, T. Neeraj, G.S. Daehn, D.H. Hou, J.M. Scott, R.W. Hayes, M.J. Mills, Mechanisms of primary creep in α/β titanium alloys at lower temperatures, Mater. Sci. Eng. A. 234–236 (1997) 996–999. doi:10.1016/s0921-5093(97)00322-5.

[19]   W.J. Evans, Optimising mechanical properties in alpha + beta titanium alloys, Mater. Sci. Eng. A. 243 (1998) 89–96. doi:10.1016/s0921-5093(97)00784-3.

[20]   Z. Zhang, F.P.E.E. Dunne, Phase morphology, variants and crystallography of alloy microstructures in cold dwell fatigue, Int. J. Fatigue. 113 (2018) 324–334. doi:10.1016/j.ijfatigue.2018.03.030.

[21]   D. Lunt, J.Q. Fonseca, D. Rugg, M. Preuss, M.S. Centre, Microscopic strain localisation in Ti-6Al-4V during uniaxial tensile loading, Mater. Sci. Eng. A. 680 (2017) 444–453. doi:10.1016/j.msea.2016.10.099.

[22]   S. Hémery, A. Naït-Ali, M. Guéguen, J. Wendorf, A.T. Polonsky, M.P. Echlin, J.C. Stinville, T.M. Pollock, P. Villechaise, A 3D analysis of the onset of slip activity in relation to the degree of micro-texture in Ti–6Al–4V, Acta Mater. 181 (2019) 36–48. doi:10.1016/j.actamat.2019.09.028.

[23] R. Bandyopadhyay, A.W. Mello, K. Kapoor, M.P. Reinhold, T.F. Broderick, M.D. Sangid, On the crack initiation and heterogeneous deformation of Ti-6Al-4V during high cycle fatigue at high R ratios, J. Mech. Phys. Solids. 129 (2019) 61–82. doi:10.1016/j.jmps.2019.04.017.

[24] T. Ben Britton, S. Birosca, M. Preuss, A.J. Wilkinson, Electron backscatter diffraction study of dislocation content of a macrozone in hot-rolled Ti-6Al-4V alloy, Scr. Mater. 62 (2010) 639–642. doi:10.1016/j.scriptamat.2010.01.010.

[25] C. Lavogiez, S. Hémery, P. Villechaise, On the mechanism of fatigue and dwell-fatigue crack initiation in Ti-6Al-4V, Scr. Mater. 183 (2020) 117–121. doi:10.1016/j.scriptamat.2020.03.031.

[26] S. Hémery, P. Villechaise, On the influence of ageing on the onset of plastic slip in Ti-6Al-4V at room temperature: Insight on dwell fatigue behavior, Scr. Mater. 130 (2017) 157–160. doi:10.1016/j.scriptamat.2016.11.042.

[27] Y. Liu, F.P.E. Dunne, The mechanistic link between macrozones and dwell fatigue in titanium alloys, Int. J. Fatigue. 142 (2021) 105971. doi:10.1016/j.ijfatigue.2020.105971.

[28] D. Rugg, M. Dixon, F.P.E. Dunne, Effective structural unit size in titanium alloys, J. Strain Anal. Eng. Des. 42 (2007) 269–279. doi:10.1243/03093247JSA273.

[29] S. Waheed, Z. Zheng, D.S. Balint, F.P.E. Dunne, Acta Materialia Microstructural effects on strain rate and dwell sensitivity in dual- phase titanium alloys, Acta Mater. 162 (2019) 136–148. doi:10.1016/j.actamat.2018.09.035.

[30] J. Qiu, Y. Ma, J. Lei, Y. Liu, A. Huang, D. Rugg, R. Yang, A Comparative Study on Dwell Fatigue of Ti-6Al-2Sn-4Zr-xMo (x = 2 to 6) Alloys on a Microstructure-Normalized Basis, Metall. Mater. Trans. A Phys. Metall. Mater. Sci. 45 (2014) 6075–6087. doi:10.1007/s11661-014-2541-5.

[31] T.S. Jun, Z. Zhang, G. Sernicola, F.P.E.E. Dunne, T.B. Britton, Local strain rate sensitivity of single α phase within a dual-phase Ti alloy, Acta Mater. 107 (2016) 298–309. doi:10.1016/j.actamat.2016.01.057.

[32] T.B. Britton, J. Jiang, Y. Guo, A. Vilalta-Clemente, D. Wallis, L.N. Hansen, A. Winkelmann, A.J. Wilkinson, Tutorial: Crystal orientations and EBSD - Or which way is up?, Mater. Charact. 117 (2016) 113–126. doi:10.1016/j.matchar.2016.04.008.

[33] C.A. Volkert, A.M. Minor, Focused Ion Beam Micromachining, MRS Bull. 32 (2007) 389–399.

[34] L.A. Giannuzzi, F.A. Stevie, Introduction to Focused Ion Beams: Instrumentation, Theory, Technique and Practice, Springer Science & Business Media, New York, 2006.

[35] Private Communication of data, under programme MAI PW-18, (2020).

[36] F.P.E. Dunne, D. Rugg, A. Walker, Lengthscale-dependent, elastically anisotropic, physically-based hcp crystal plasticity: Application to cold-dwell fatigue in Ti alloys, Int. J. Plast. 23 (2007) 1061–1083. doi:10.1016/j.ijplas.2006.10.013.

[37] Z. Zhang, T.S. Jun, T.B. Britton, F.P.E. Dunne, Intrinsic anisotropy of strain rate sensitivity in single crystal alpha titanium, Acta Mater. 118 (2016) 317–330.

doi:10.1016/j.actamat.2016.07.044.

[38]   M.F. Ashby, The deformation of plastically non-homogeneous materials, Philos. Mag. 21 (1970) 399–424. doi:10.1080/14786437008238426.

[39]   S. Nemat-Nasser, W.G. Guo, J.Y. Cheng, Mechanical properties and deformation mechanisms of a commercially pure titanium, Acta Mater. 47 (1999) 3705–3720. doi:10.1016/S1359-6454(99)00203-7.

[40]   K. Kirane, S. Ghosh, A cold dwell fatigue crack nucleation criterion for polycrystalline Ti-6242 using grain-level crystal plasticity FE Model, Int. J. Fatigue. 30 (2008) 2127–2139. doi:10.1016/j.ijfatigue.2008.05.026.

[41]   T.S. Jun, D.E.J. Armstrong, T.B. Britton, A nanoindentation investigation of local strain rate sensitivity in dual-phase Ti alloys, J. Alloys Compd. 672 (2016) 282–291. doi:10.1016/j.jallcom.2016.02.146.

[42]   B. Ellis, R. Smith, Polymers: a Property Database, 2008.

[43]   Y. Xiong, P. Karamched, C. Nguyen, D.M. Collins, Cold Creep of Titanium : Analysis of stress relaxation using synchrotron diffraction and crystal plasticity simulations, SSRN Electron. J. n. Pag. Crossref. Web. (2020).

[44]   F. Bachmann, R. Hielscher, H. Schaeben, Grain detection from 2d and 3d EBSD data-Specification of the MTEX algorithm, Ultramicroscopy. 111 (2011) 1720–1733. doi:10.1016/j.ultramic.2011.08.002.

[45]   M.A. Groeber, M.A. Jackson, DREAM . 3D : A Digital Representation Environment for the Analysis of Microstructure in 3D, Integr. Mater. Manuf. Innov. 3 (2014) 1–17. doi:10.1186/2193-9772-3-5.

[46]   Z. Zhang, T.S. Jun, T.B. Britton, F.P.E. Dunne, Determination of Ti-6242 α and β slip properties using micro-pillar test and computational crystal plasticity, J. Mech. Phys. Solids. 95 (2016) 393–410. doi:10.1016/j.jmps.2016.06.007.

[47]   Z. Zhang, D. Lunt, H. Abdolvand, A.J. Wilkinson, M. Preuss, F.P.E. Dunne, Quantitative investigation of micro slip and localization in polycrystalline materials under uniaxial tension, Int. J. Plast. 108 (2018) 88–106. doi:10.1016/j.ijplas.2018.04.014.

[48]   Z. Zheng, D.S. Balint, F.P.E. Dunne, Discrete dislocation and crystal plasticity analyses of load shedding in polycrystalline titanium alloys, Int. J. Plast. 87 (2016) 15–31. doi:10.1016/j.ijplas.2016.08.009.

[49]   R. Demott, P. Collins, C. Kong, X. Liao, S. Ringer, S. Primig, a3D electron backscatter diffraction study of α lath morphology in additively manufactured Ti-6Al-4V, Ultramicroscopy. (2020) 113073. doi:10.1016/j.ultramic.2020.113073.

[50]   M.D. Sangid, J. Rotella, D. Naragani, J. Park, P. Kenesei, P.A. Shade, M.D. Sangid, J. Rotella, D. Naragani, J. Park, A complete grain-level assessment of the stress-strain evolution and associated, Acta Mater. (2020). doi:10.1016/j.actamat.2020.09.051.

[51]   Z. Zheng, A. Stapleton, K. Fox, F.P.E. Dunne, Understanding thermal alleviation in cold dwell fatigue in titanium alloys, Int. J. Plast. 111 (2018) 234–252. doi:10.1016/j.ijplas.2018.07.018.

[52] I.P. Jones, W.B. Hutchinson, Stress-state dependence of slip in Titanium-6Al-4V and other H.C.P. metals, Acta Metall. 29 (1981) 951–968. doi:10.1016/0001-6160(81)90049-3.

[53] M.A. Cuddihy, A. Stapleton, S. Williams, F.P.E. Dunne, On cold dwell facet fatigue in titanium alloy aero-engine components, Int. J. Fatigue. 97 (2017) 177–189. doi:10.1016/j.ijfatigue.2016.11.034.

[54] D. Rats, L. Vandenbulcke, C. Boher, G. Farges, Tribological study of diamond coatings on titanium alloys, 94–95 (1997) 555–560. doi:10.1016/S0257-8972(97)00465-9.